Additive Manufacturing 46 (2021) 102148

Contents lists available at ScienceDirect

Additive Manufacturing

journal homepage: www.elsevier.com/locate/addma

Down-facing surfaces in laser powder bed fusion of Ti6Al4V: Effect of dross formation on dimensional accuracy and surface texture

Amal Charles [a,*], Ahmed Elkaseer [a,b], Umberto Paggi [c,d], Lore Thijs [c], Veit Hagenmeyer [a], Steffen Scholz [a,e,f]

[a] Institute for Automation and Applied Informatics (IAI), Karlsruhe Institute of Technology (KIT), 76344 Eggenstein-Leopoldshafen, Germany
[b] Department of Production Engineering and Mechanical Design, Faculty of Engineering, Port Said University, Port Fuad 42526, Egypt
[c] Direct Metal Printing Engineering, 3D Systems, 3001 Leuven, Belgium
[d] KU Leuven, Department of Mechanical Engineering, 3001 Leuven, Belgium
[e] Karlsruhe Nano Micro Facility, Hermann-von-Helmholtz-Platz 1, 76344 Eggenstein-Leopoldshafen, Germany
[f] Future Manufacturing Research Institute, College of Engineering, Swansea University, Swansea SA1 8EN, UK

ARTICLE INFO

Keywords:
Laser powder bed fusion
Ti6Al4V
Down-facing surfaces
Dross formation
As-built quality

ABSTRACT

Down-facing surfaces are one of the most challenging features in metal parts produced by laser powder bed fusion (LPBF). A combination of reasons, primary of which are residual stresses and overheating cause these features to have the worst surface finish and dimensional accuracy of all LPBF surfaces. In order to examine this phenomenon, a Design of Experiments (DoE) study is conducted for three different inclination angles, namely 45°, 35° and 25° and for two different layer thicknesses of 60 μm and 90 μm. The results from the DoE are used to establish quadratic regression equations that can be used to predict the quality marks of surface roughness and the relative dimensional error.This fundamental investigation helps to explain the reasons for the major defects in down-facing surfaces of parts produced with Ti-6AL-4 V material, namely the dross formation and attempts to improve the predictability of quality within the region. Further to the establishment of the quadratic equations, a discussion is conducted on the thermomechanical processes involved in the mechanism of dross formation and explanations are given on the reasons behind the observed physical phenomena. The trend of the propagation of (Root Mean Square) RMS Surface roughness (*Sq*) and the relative dimensional error with respect to the Volumetric Energy Density (VED) is discussed in detail. The respective quadratic equations are then tested by a second round of validation prints, and the results confirm the feasibility of the developed quadratic models to accurately predict process outcomes especially when operating near the suggested optimal printing zones. The high roughness of low VED printing is attributed to the formation of 'inverse mushroom' structures, and the low roughness of high VED surface is attributed to the formation of large flat regions formed as adjacent meltpools that can fuse together at various locations.

1. Introduction

Additive Manufacturing (AM) technologies refer to the processes of layer-by-layer manufacturing that are creating a new paradigm in the way parts are produced and value is added to new/modified products [1]. This is largely due to the benefits offered by AM technology in terms of both scale and scope [2,3].

Down-facing surfaces (as seen in Fig. 1) of the L-PBF process are especially critical. They typically have the worst surface quality of all surfaces made by L-PBF processes and are a host to many defects such as porosities induced due to keyhole mode melting [4,5], and research efforts in this field are being made in order to address the issues faced. However, significant gaps still exist in fully understanding the fundamentals of the L-PBF process in the down-facing region. Patterson et al. [6] studied 143 different publications related to the L-PBF process and concluded that only a small minority deals particularly with the overhanging problem, where only limited fundamental work has been done.

The issue of residual stresses caused by the repeated cycling of heat input by the laser scanning across each layer and on top of solidified material, causing remelting, is well known for the L-PBF process.

* Corresponding author.
E-mail addresses: amal.charles@kit.edu (A. Charles), ahmed.elkaseer@kit.edu (A. Elkaseer), umberto.paggi@3dsystems.com (U. Paggi), lore.thijs@3dsystems.com (L. Thijs), veit.hagenmeyer@kit.edu (V. Hagenmeyer), steffen.scholz@kit.edu (S. Scholz).

https://doi.org/10.1016/j.addma.2021.102148
Received 4 February 2021; Received in revised form 22 June 2021; Accepted 24 June 2021
Available online 29 June 2021

Mercelis and Kruth [7] have explicitly described the specific mechanics of stress formation in the L-PBF Process as being caused by the formation of two zones of large tensile stresses at the top and bottom of the parts while there exists a large zone of intermediate compressive stresses in between in the bulk of the part. Post-process heat treatment is generally used as a method in order to minimize the adverse effects of residual stresses such as warping. Maleki et al. reviewed in detail various post treatment for metal AM and the opportunities offered by them in order to improve as-built surface quality in inclined surfaces [8].

Overhanging features are not printed with direct connections to the build plate, therefore the issue of residual stress is a big factor, which is further affected by their inability to conduct heat away from the part, leading to large overheated zones [9]. Therefore the most common methods of avoiding problems with overhanging features include the usage of solid support structures, redesign of part geometry, or reorientation of the part in the build platform [10], which all have the potential to cause issues related to increased cycle time, increased post-processing time, increased material usage, decreased surface finish quality, damages caused by support removal processes and even build failures. Jhabvala et al. [11], Wang and Chou [12] as well as Calignano [13] discussed the above mentioned issues related to fabrication of support structures.

Therefore, the research related to the study of down-facing surfaces has been quite diverse in terms of the approaches used, with some researchers focusing on optimized design of support structures or of the overhanging features itself while others have focused on process parameters optimization thereby adopting statistical approaches to understanding the process. Elkaseer et al. [14] reviewed 140 papers to highlight the process based challenges to precision in AM processes and suggest reliable approaches for the development of precise AM processes. However, building of specific process models for the LPBF process within the down-facing area is not a well explored topic, though general process models for the LPBF process as a whole do exist. Kruth et al. [7] developed one such model for the LPBF process, while Markl and Körner [15] used a numerical modelling approach to describe the LPBF process. Bayat et al.[16] have conducted high fidelity modelling and validation for key-hole induced porosities in LBPF. The modelling and simulation of the LPBF process at down-facing regions is therefore still at early stages of investigation and development.

When it comes to down-facing regions, it is a widely accepted practice that an angle of 45° is usually the lower limit, when it comes to being able to guarantee high quality and stable prints, and below which support structures are required [10]. In order to counteract some of the negative aspects of support structures, some research has also gone into the development of optimized support structures. Cooper et al. [17] developed contact free support structures that required little to no post processing and their proof of concept was able to demonstrate its feasibility for further application. Paggi et al. [18] developed another type of contact-less support which was supplemented by numerical modelling techniques in order to determine the optimal distance between the support and the part. Calignano [13] conducted design optimization of support structures using the Taguchi method in order to provide optimal parameters for a self-supporting design of parts. However, along with the self-supporting structures the reorientation of parts was suggested as necessary in order to minimize the usage of supports as much as possible.

Next to the design optimization of support structures, design optimization of overhanging parts itself is a popular topic. A number of different works have developed frameworks for the inclusion of an overhang constraint for the designing of parts by topology optimization. Driessen et al. [19] developed an overhang constraint for topology optimization that showed promise especially with the inclusion of build orientation as a constraint. Garaigordobil et al. [20] were able to employ the parameter of maximum allowable inclination angle in their overhang constraint for the designing of self-supporting structures. Ranjan et al. [21] presented a physics based approach for integration and detection of heat accumulation within a topology optimization framework, in an attempt to address the thermal aspects of AM during the design stage itself.

The energy density applied on the powder by the laser has previously been suggested as a parameter for characterising the L-PBF process [22]. This is because the energy density is a factor that affects a whole range of phenomena such as the melt-pool dimensions (as length, depth, flow ability and viscosity), which affects the way the metal powder interacts with each other, the meltpool, the adjacent layers and features. Khorasani et al. [23] included energy density in their investigation on the effect of different L-PBF process parameters on part density, hardness, tensile strength and surface quality and their results showed correlation between hardness, density and meltpool formations. King et al. [24] concluded that the energy density of the laser beam controls the transition from a conduction-mode to keyhole-mode melting in the L-PBF process, while some advocate the usage of energy density due to its ability to capture track width evolution and the normalized melt pool depth [22, 25–28].

However, Bertoli et al. [29] on their investigation on the usage of Volumetric Energy Density (VED) for 316LSS parts recommend caution on its usage as a design parameter due to its narrow band of applicability, which they attributed to its inability to capture complex melt pool

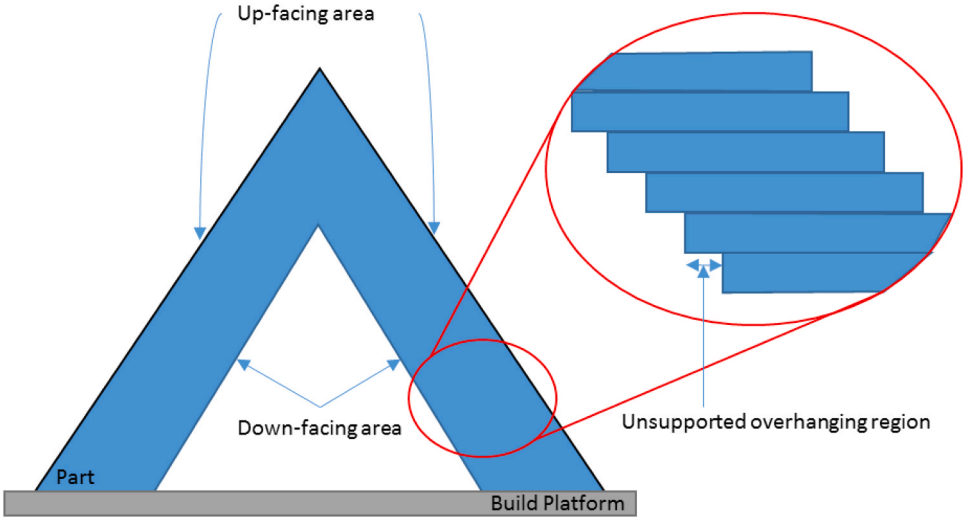

Fig. 1. Down-facing and up-facing areas in L-PBF parts, and the unsupported overhanging regions.

physics, though they also mention that the track width generally increases with increasing VED and that VED is useful in calculating the amount of energy delivered per unit volume on the powder bed. Caiazzo et al. on their investigation of VED for Inconel 718 in LPBF conclude that VED remains a statistically significant parameter that can be used confidently for process design and optimization[30]. Since this research work is focused on dross formation, which is caused directly as a result of the degree of overheating, it was decided to also present the trends in relative dimensional error and Sq with relation to the VED within the down-facing region and we merely used it to investigate its applicability within the down-facing area of TI6al4V parts. Dross is defined as excess material that is present on overhangs caused by excessive melting as a results of overheating within the down-facing area. The VED (*Ev*) is generally a thermodynamic quantity and is shown in Eq. (1):

$$E_V = \frac{P}{vht} \quad [\mathrm{J}/mm^3] \tag{1}$$

where P denotes the power of the laser in W, v denotes the scan speed in mm/s, h denotes the hatch spacing in mm and t denotes the layer thickness in mm. VED has been used by a number of research works focused on LPBF in order to classify surface roughness of AM parts produced with various materials [31].

Many applications still require and would benefit from an improved fundamental understanding of down-facing surfaces, which would enable the printing of features or structures that have low angles, at locations where supports or any other kind of reorientation would not be possible. As discussed above, a number of research attempts have focused on the critical features that are the down-facing surfaces. The major physical defect in down-facing surface is due to the presence of large dross formations, which create large dimensional deviations and high surface roughness. Higher surface roughness can be undesirable and can progressively decrease the performance of LPBF parts as additionally to increasing the dimensional inaccuracy, it also affect mechanical performance such as fatigue performance, this is described by Pegues et al. [32] and Razavi et al. [33]. This causes the increase in disapproval of using LPBF systems for many new applications. However, understanding the effect of different process parameters on the quality of these surfaces, and qualitatively analyzing this phenomenon to understand the underlying behavior of printing in down-facing regions has received little attention so far. Shange et al. investigated the roughness and near-surface porosity in down-facing surfaces produced by high speed LPBF and concluded that both roughness and porosity vary as a function of the inclination angle [34].

Charles et al. in a previous work [9] have conducted an introductory investigation on the trends related to surface roughness in down-facing surfaces. Their findings merely depict the general trends on how surface roughness varies within a range of process parameters. However, there was no fundamental explanation provided about the physical phenomenon behind the seen dross formation and its causative effect on surface roughness. This clearly indicates a real need for a comprehensive study describing the progression of dross formation within the overhanging region, and the characteristics surface features that are responsible for the high and low surface roughness along with their formative mechanisms.

In this context, the aim of the present paper is to bridge this gap by investigating dross formation in down-facing surface made of Ti-6Al-4V. Correlations between Volumetric Energy Density (VED) and the dimensions of the melt pool formed have been stated by others, and according to our expectations, the depth and penetration of the meltpool is the major reason for dross formation and hence for defects in down-facing surfaces. Therefore, the present work will attempt to unravel the nature of the relationship between VED and the resultant quality of surfaces and the applicability of VED within the down-facing region. Experimental trials are conducted following a Design of Experiments (DoE) within the down-facing region, and models based on regression are developed and then validated by conducting further printing experiments. The regression models can be used to make predictions on the chosen performance indicators. Scanning Electron Microscope (SEM) images and microscopy imaging of cross cuts provide further insight on the topography of the surfaces formed under different printing conditions and correlations are made with respect to the process parameters.

2. Materials and methods

The present work's approach towards understanding the dimensional accuracy and surface quality of down-facing surfaces is by utilizing a down-facing printing strategy where special process parameters and scanning patterns are applied only within immediately adjacent volume of the down-facing surface, see Fig. 2(a) and (b). This ensures that the rest of the part can still be built using other standard, qualified and validated parameters while down-facing surfaces are individually targeted. The novelty in building predictive process models is that it allows the tailoring of surface quality within down-facing surfaces. For instance, parts that might have different surface roughness at different locations can be built in one build, with tailored process parameters for the down-facing surfaces while the rest of the part is built with standard process parameters. The latter might focus on improving the productivity or density, whereas the down-facing parameters target lowest surface roughness. This work compares three different overhang angles 45°, 35° and 25° and attempts to build models for each of these angles.

2.1. Design of experiments

For the regression modelling conducted in this work, an inscribed central composite design is utilized. This type of design is utilized specifically when the limits for the various input factors of a process are known and five levels for each factor are required. The input parameters chosen to model the process and the five levels of each parameter can be seen in Table 1. The ranges of the laser power and scan speed are chosen very widely and cover a large area of the typical process parameters for L-PBF. However, the ranges are also chosen based on the informed suggestions of the process development experts from 3DSystems as well as through conducting preliminary experiments within expected ranges where optimal ranges may be found and to confirm that parts can be safely printed within the complete chosen ranges. Once the extremes of the range were decided, the in-between levels were automatically generated based on the range and the DoE was modelled and performed on Matlab (Mathworks, Version R2019a) using the Statistics toolbox. The DoE as used in the first phase can be seen in Table 2.

As seen in Table 2. The factor settings are identified as required for a central composite inscribed design (CCI), For the CCI design, extreme points are already set and the trials 1–8 are the factorial points in the design, trials 9–14 are the star points while the trials 15–24 are the system-recommended center points and are repeated nine times for a high confidence. Included with the process parameters laser power, scan speed and scan spacing are the discrete parameters of scanning pattern and layer thickness. Since a total of 3 scanning patterns and 2 layer thicknesses are investigated, the DoE seen in table is conducted for each scanning pattern and repeated for each layer thickness, thus leading to the printing of 144 samples for each angle (72 samples for 60 μm layer thickness and 72 samples for 90 μm layer thickness). All test pieces were printed at the focal plane of the laser and the laser spot size was therefore kept constant over the whole experimental trials.

2.2. Test piece design

Test pieces are designed having overhang angles of 45°, 35° and 25°. This is because at the current state-of-the-art, 45° represents the limit below which the surface quality and dimensional accuracy deteriorates below acceptable levels. Therefore, improving the as-built quality of 45° overhanging parts and additionally also of 35° and 25° overhangs

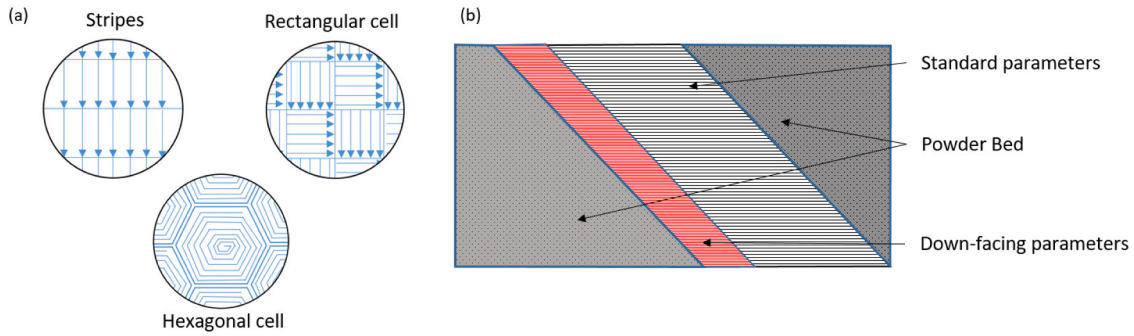

Fig. 2. Illustration of (a) the different scanning strategies and (b)the down-facing printing strategy and region where down-facing parameters are used.

Table 1
Levels of the different process parameters.

Process parameter	Levels
Laser Power [W]	50, 90, 150, 210, 250
Scan Speed [mm/s]	200, 465, 850, 1235, 1500
Scan Spacing [μm]	50, 60, 75, 90, 100
Scanning Pattern [-]	Strips, Rectangular cells, Hexagonal cells
Layer thickness [μm]	60, 90

Table 2
Experimental design for Phase 1.

Trial	Laser Power [W]	Scan Speed [mm/s]	Scan Spacing [μm]
1	90	465	60
2	90	465	90
3	90	1235	60
4	90	1235	90
5	210	465	60
6	210	465	90
7	210	1235	60
8	210	1235	90
9	50	850	75
10	250	850	75
11	150	200	75
12	150	1500	75
13	150	850	50
14	150	850	100
15–24	150	850	75

represents significant progress to the current state-of-the-art in achievable quality of metal AM parts. The printed test pieces and their dimensions can be seen in Fig. 3. Each test piece has a down-facing surface area of 200 mm^2 (20 mm in length and 10 mm width) which provides a large enough surface area for effective characterization of surface texture as well as to conduct sufficient repetitions to ensure a high level of confidence on the measurement.

2.3. L-PBF System and material

For the present work, all test pieces are printed using a 3D Systems ProX® DMP 320, a popular industrial metal AM system based on L-PBF. The material used in this study is LaserForm Ti Gr23 (A) powder (Ti-6Al-4V) with a PSD of 15–45 μm, which is a commonly used Titanium alloy for usage in aerospace and medical applications and is known for its high strength, low weight and biocompatibility. The 3DXpert Software for Pre-processing from 3D Systems is used for pre-processing of the samples before production. This includes setting the parameters within the down-facing area as well as the bulk of the part, positioning and orientation of parts and slicing.

2.4. Characterisation

Within the down-facing surface, two parameters are used to determine the quality of the print. The first being the dimensional accuracy and the second is the surface texture. The thickness of the overhang is directly affected by process parameters and therefore is used to analyse the dimensional deviation. The dimensional deviation is represented as percentage deviation of the printed part in comparison to the CAD design of the part.

In order to analyse the surface texture of the down-facing area, a number of surface parameters are initially investigated and the parameter root mean square roughness *Sq* is chosen as the quality parameters in order to conduct the statistical modelling study. The Sq parameter was chosen as it is a commonly used surface texture parameter, and it was the suggestion based on conversations with metrology experts as well as industrial partners where the parameter is used as well. The trend of Sq in relation with Sa is reported to be consistent and the Sq

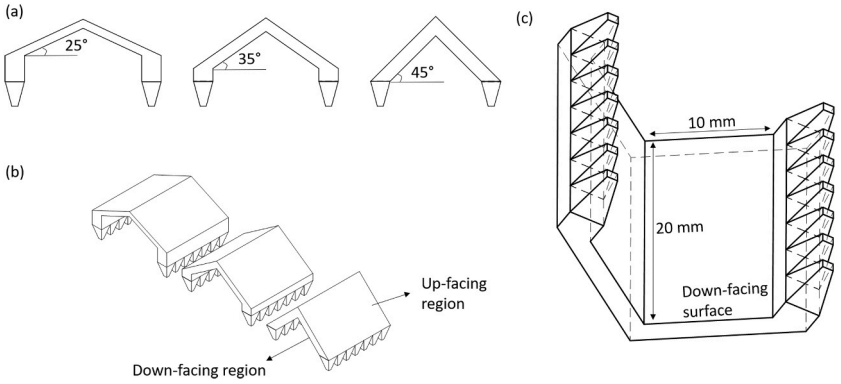

Fig. 3. (a) Front view of manufactured test pieces showing all three printed angles (25°, 35° and 45°), (b) isometric view of printed test pieces and (c) view of down-facing surface of all test pieces.

parameter has been used in recent research works focussed on the LPBF process and has been found to be illustrative for understanding the surface texture of AM surfaces [35]. The usage of Sq (and Sa) have been correlated to the presence of porosity and the usage of these parameters within this study was done with the objective to present the surface texture results in a parameter that is commonly used in industry and academia to therefore can give a quick idea to users. Due to the nature of the overhanging surface being highly irregular and with a random distribution of peaks and valleys, it is decided against using a height based parameter such as *Sz* (Maximum height*)*.

In order to characterize the surfaces, all samples are measured using a focus variation microscope (Manufacturer Sensofar, Model - S Neox). The down-facing surface on each sample is measured 5 times at distinct different locations as seen in Fig. 4(a). Each single measurement measured an area of 2.3 mm * 3.1 mm (7.13 mm^2) leading to a total measured area of 35.65 mm^2 on each sample, which is a significant area of measurement.

In order to obtain the roughness component of the measured surface, the MountainsMap Expert software is used (Version 8, DigitalSurf) and the ISO 25178 workflow for surfaces is followed. The extracted surface from the focus variation microscope is then filtered using an S Filter of 2.5 μm (For removing small scale components) followed by an F operator (for removing the form and levelling the surface by subtracting the least-squares mean plane) and an L filter of 0.25 mm (which removes large scale components). The resultant surface (SL Surface) is the one used for retrieving the roughness parameters such as *Sq*.

Dimensional measurements are made using a Keyence VHX 7000 digital microscope and each thickness measurement is repeated 5 times at 5 different locations for each sample as seen in the Fig. 4(b). The measured thicknesses of the test pieces are then compared with the expected thickness from the CAD design. The difference in the measurement allows the calculation of the dimensional error of each test piece. The percentage deviation of the measured thickness from the CAD design thickness is used to calculate the relative dimensional error of each part. For the dimensional measurement, each test piece was scanned with a magnification of 100X and the individual images were stitched together to gather the image of the complete test piece. The surface texture maps were also scanned with a magnification of 100X and stitched. Additionally, cross cuts of selected samples representing different energy densities (High, Low and Optimal) were made. The samples were polished and analysed under the Keyence and Sensofar microscope in order to examine the surface and near surface defects and morphologies of the different energy densities.

A Scanning Electron Microscope (TESCAN VEGA3) is then used to investigate in depth the nature of the surface texture, such as the generated dross in down-facing surfaces, and to investigate the different representative features that help to characterise optimal as well as defective surfaces. The SEM images were focussed on capturing the characteristic features noticeable on the surface of different test pieces. Therefore firstly the top view was investigated in a similar fashion to the roughness measurements and secondly to capture the longer penetrations of the meltpool the part was oriented in order to capture it best.

3. Results

The initial observations on the three different down-facing surfaces (45°, 35° and 25°) are based on the measured values of the relative dimensional error and the measured Root Mean Square surface roughness (*Sq*). The graphs for the 45° surface are shown in Figs. 5, 6, 7 and 8, while the graphs for the 35° and 25° down-facing surface can be seen in the Appendix in Figs A.1 to A.8.

Figs. 5 and 6 depict the measured values of the dimensional error % and surface roughness (*Sq*), respectively, for 45°overhangs with 60 μm layer thickness, while Figs. 7 and 8 present measured dimensional error % and surface roughness (*Sq*), respectively, for 45°overhangs with 90 μm layer thickness.

As can be seen in Figs. 5, 6, 7 and 8, within the current data set, samples with high laser power and a low scan speed show high relative dimensional error and low *Sq*, while samples with low laser power and high scan speed show high *Sq* and low relative dimensional error, which lends credence to the continuation of the usage of volumetric energy density as a combined parameter for characterisation of down-facing surfaces within the present work. This is also the case for the angles of 35° and 25° as can be seen from the graphs in Figs. A.1 to A.8.

Furthermore, other research efforts report the influence of scan strategy on the final quality of L-PBF parts [36,37]. However, the effect of the three different scan strategies within the current work is expected to be minimal as the effective area where the scan patterns are varied is miniscule when compared to the global strategy, which doesn't allow any considerable effect to propagate as a result of different scan strategies within the down-facing area [38]. This becomes evident as the measured values of *Sq* and relative dimensional error for the three

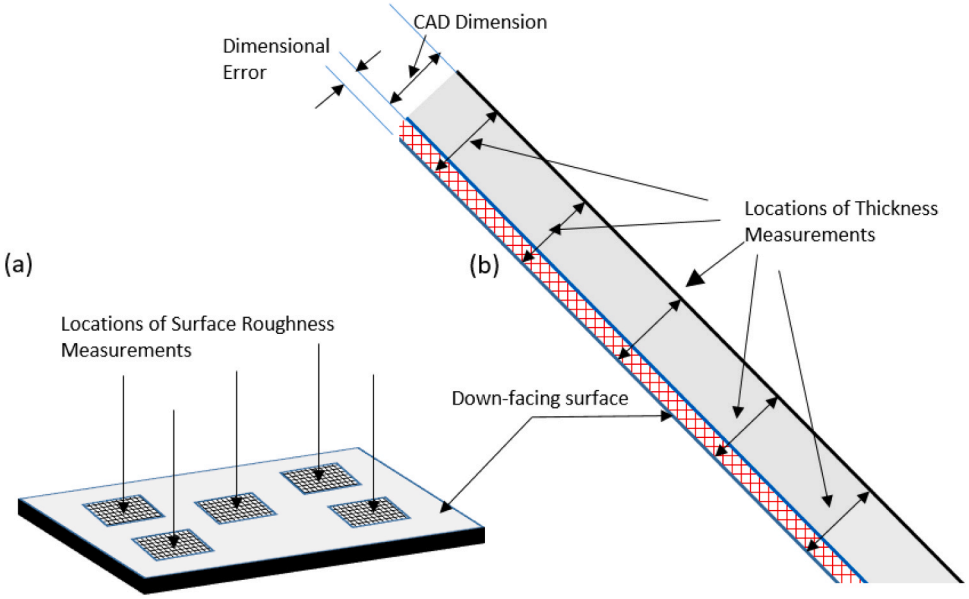

Fig. 4. locations where the surface roughness measurement and thickness measurement of test pieces were made.

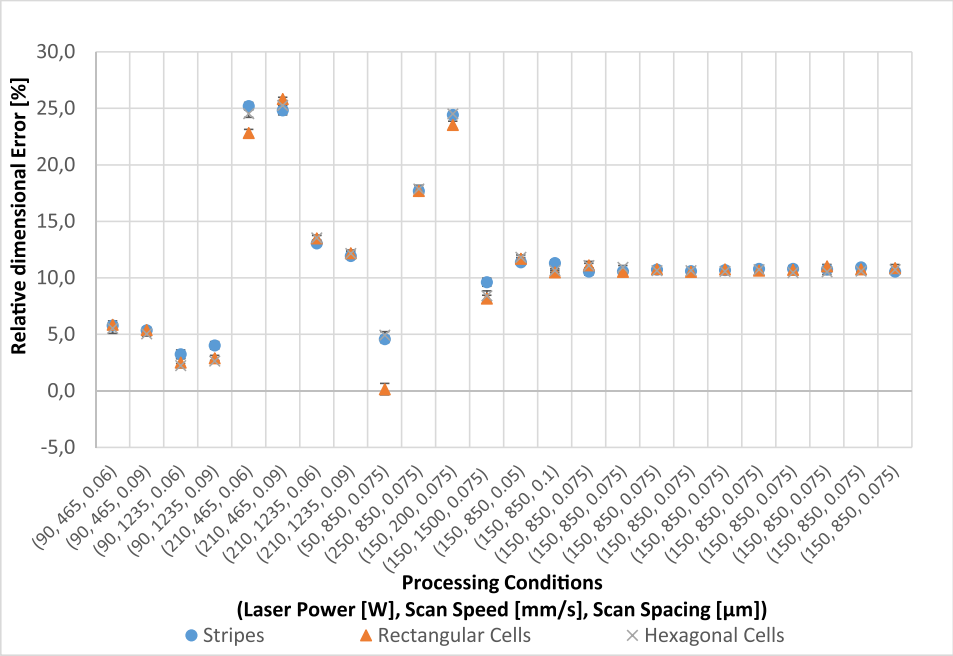

Fig. 5. Relative dimensional error for 45° overhang angles at 60 µm Layer Thickness.

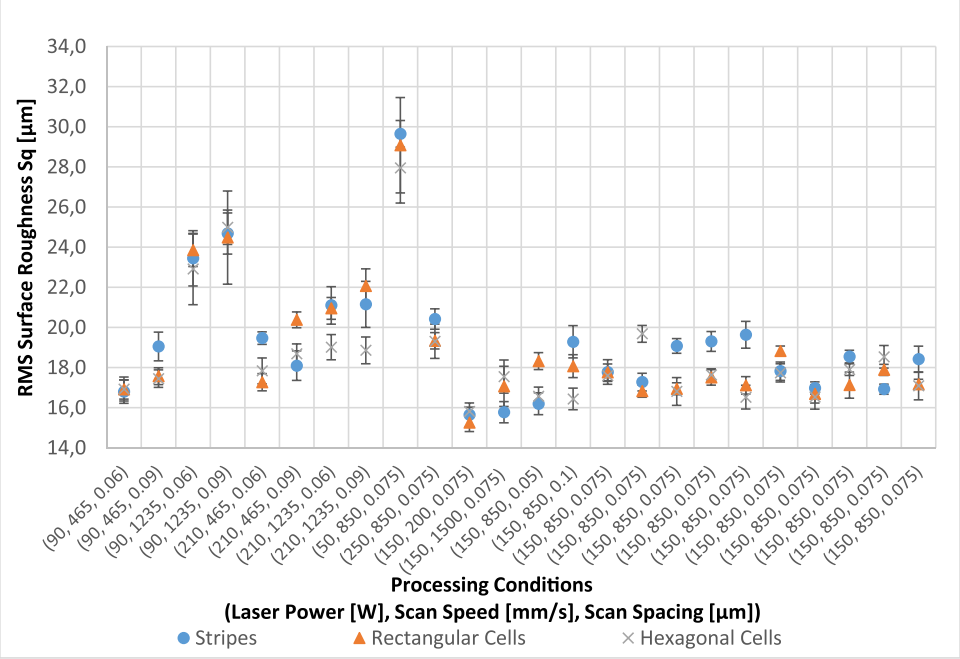

Fig. 6. RMS surface roughness of 45° overhang angles at 60 µm layer thickness.

different scan strategies, albeit displaying certain outliers, are similar. The differences in the measurements can be attributed to the irregular surface formed as a result of the L-PBF process being operated in certain unstable parameter combinations. Therefore the effect of scan strategy can be considered to be minimal for both *Sq* and relative dimensional error for all angles.

Down-facing surfaces are generally present with different artefacts and defects such as spatter, which lends to the surfaces being unstable or harder to characterise. Still, the error bars for the measured *Sq* show that the variation in the surface between samples with different scan strategies is quite minimal: The error bars for the *Sq* measurements are slightly larger than the ones for the dimensional error %, and this is explained as since five measurements are made on each sample in different locations, the non-uniform nature of down-facing surfaces contributes to this slightly larger error bar for surface roughness (Approx. maximum ± 4 µm) as seen in Figs. 6 and 8. This is also the case for the 35° and 25° down-facing surfaces as seen in the Appendix. Finally, the centre points of the DoE (150 W, 850 mm/s, 75 µm) show excellent repeatability in dimensional and surface quality, thereby pointing towards a robust stable process that can be modelled and thereby predicted.

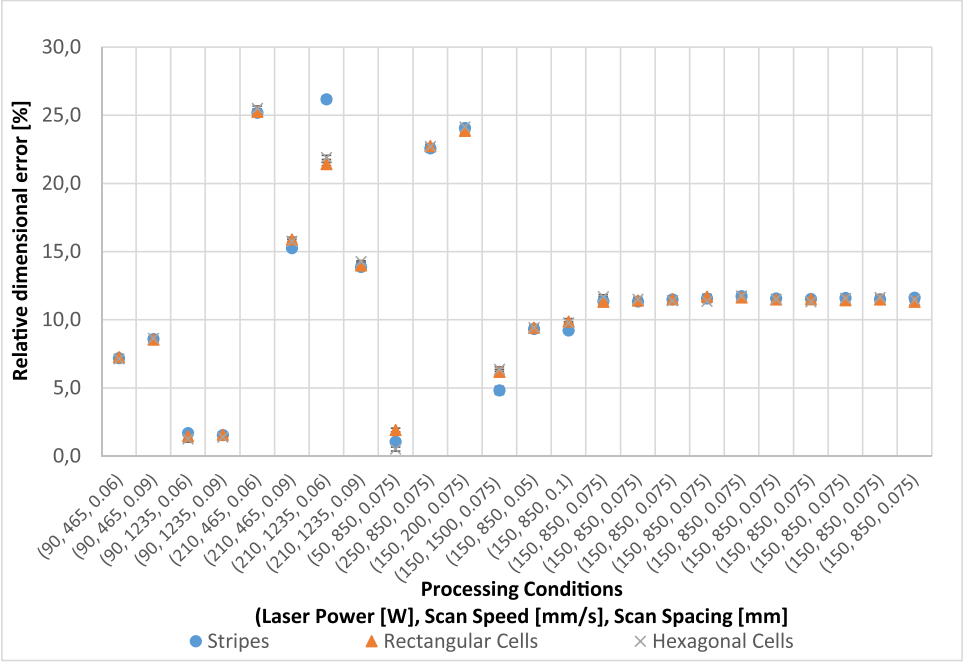

Fig. 7. Relative dimensional error of 45° overhang angles at 90 μm layer thickness.

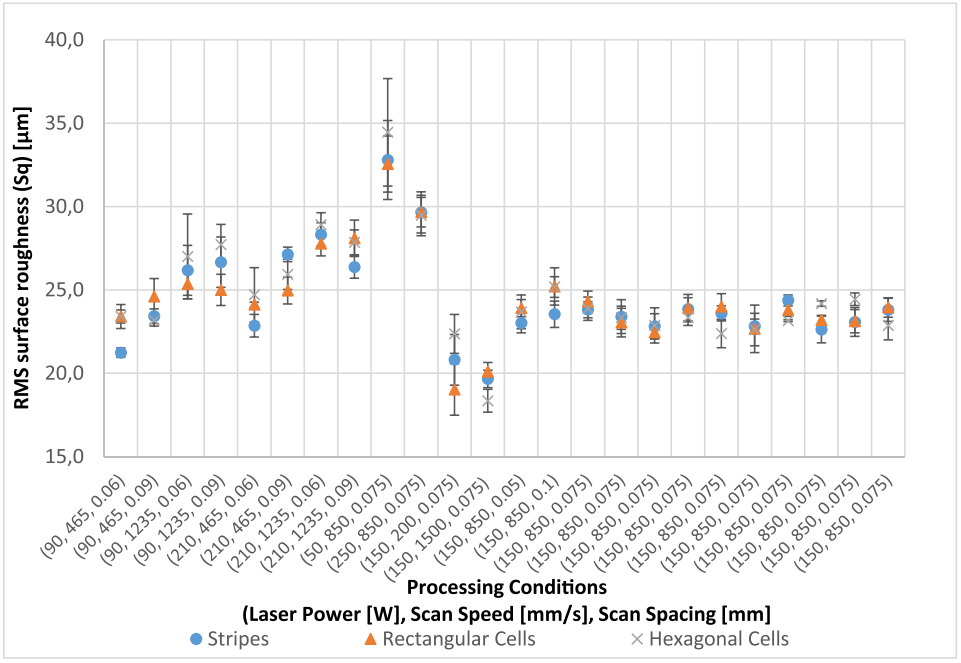

Fig. 8. RMS surface roughness of 45° overhang angles at 90 μm layer thickness.

3.1. *Down-facing surfaces of 45°*

Graphs depicting the behaviours of the *Sq* and relative dimensional error with respect to the volumetric energy density (VED) are plotted in Figs. 9 and 10, with the *Sq*, relative dimensional error and VED for the 45° down-facing parts printed with 60 μm and 90 μm layer thicknesses, respectively. For the sake of clarity, only the results from the scanning pattern 'stripes' are shown, however the discussed trends are valid for all scanning patterns, as the influence of scanning pattern on the dimensional accuracy and surface roughness is minimal. A trend line with a logarithmic fit been added to visualize the trend of the relative dimensional error and *Sq* in the Y axis compared to the VED along the X Axis. The logarithmic trend line is used since physically it describes the seen phenomenon, when increasing the VED i.e the dimensional error keep increasing (due to larger dross formations due to increased overheating) and the Surface roughness keeps decreasing until the measured roughness reaches the size of the powder particles. It is observed that the rate of change of surface roughness and dimensional error is higher at first and begins to level out as the VED is increased, therefore the logarithmic trendline is able to describe this phenomenon well.

Observing the graphs in Figs. 9 and 10, the indications are very interesting, considering that these results are valid only for 45° overhangs. Firstly, it becomes evident that for both the 60 μm and 90 μm layer thickness processes, the trend of the relative dimensional error is in

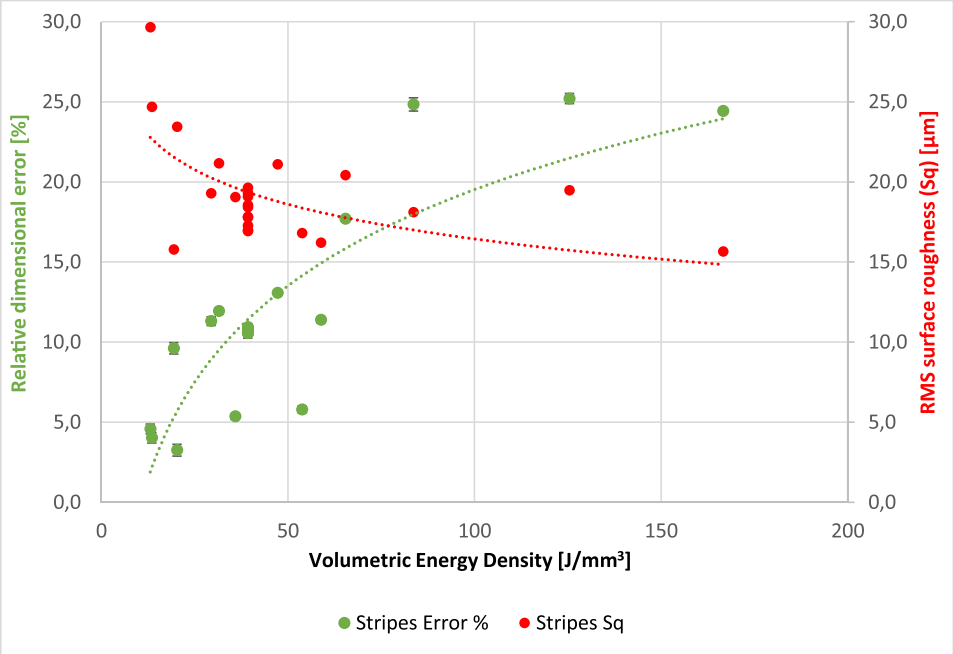

Fig. 9. Trends between relative dimensional error, Sq and VED for 45° samples with 60 µm layer thickness.

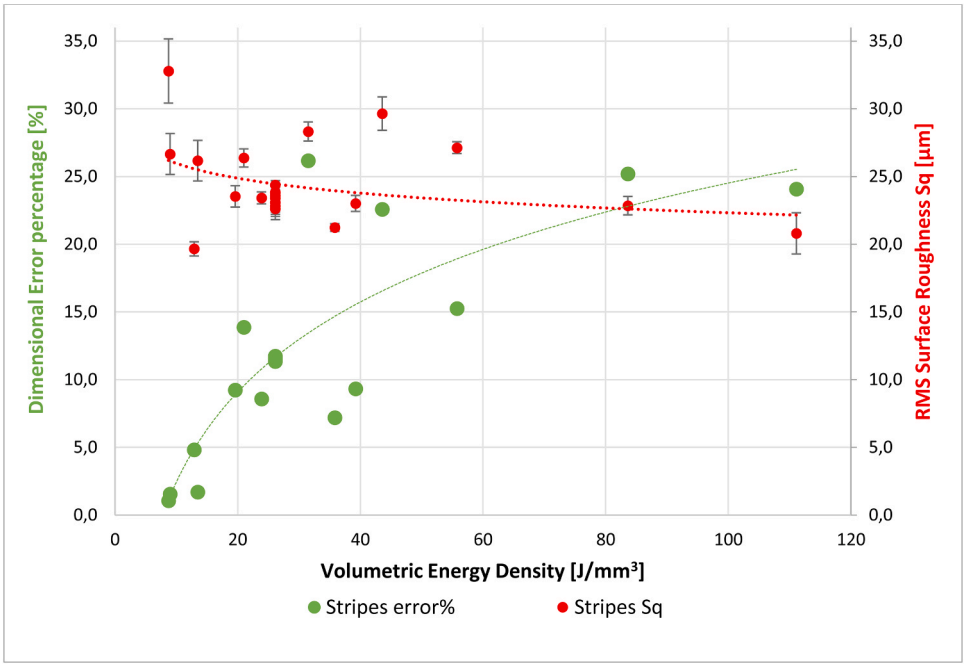

Fig. 10. Trends between relative dimensional error, Sq and VED for 45° samples with 90 µm layer thickness.

general increasing with an increase in VED. For both 60 µm and 90 µm layer thickness the surface roughness decreases while increasing the VED. Furthermore, for both the 60 µm and 90 µm layer thicknesses the region of 30–50 J/mm^3 represents a region where the relative dimensional error is at its least while the *Sq* is also at the least and is therefore is an indication as to an optimal process window for the printing of low surface roughness, low relative dimensional error at 45°overhangs surfaces.

From the series of images in Fig. 11, the formation of the dross on the down-facing surface can be qualitatively explained. In Fig. 11 (a), the VED applied by the laser on the down-facing area is low and previous research works have explained the correlation between VED and the track width of the melt pool [22] as well as the degree of overheating. A smaller meltpool resulting in a smaller heat affected zone results in minimal penetration of the meltpool into the powder bed, which causes the dross formation to be small in size and thereby explaining the lower relative dimensional error depicted in Figs. 9 and 10. This is also attributed to the hydrodynamic instability of the melt driven by the Marangoni effect due to the low VED, as the range of a stable melt pool zone decreases at low laser powers and high speeds [39,40], which is true for the part in Fig. 11 (a). One can argue that in certain locations the edges of the heat affect zones (HAZ) also do not exhibit a high enough temperature to sufficiently melt surrounding powder particles, thereby creating the random distribution of flat molten powder free regions seen

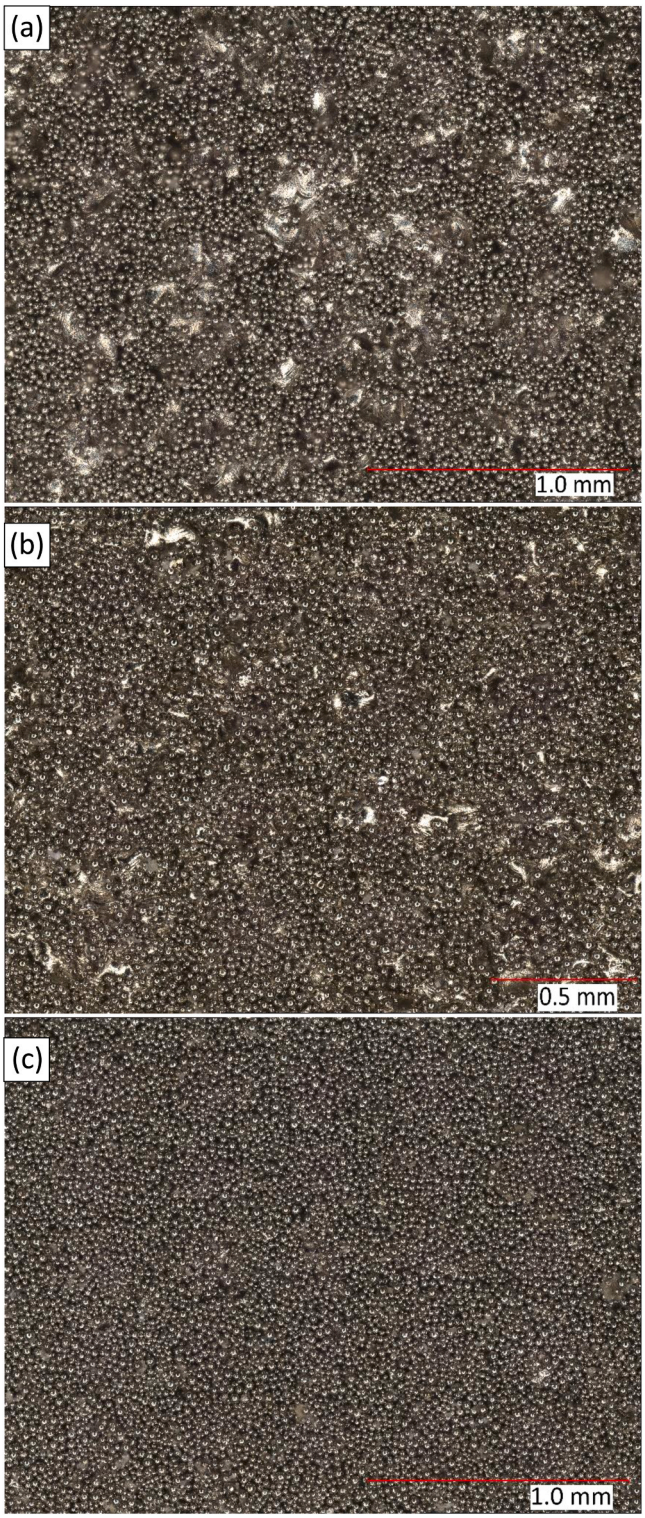

Fig. 11. Top view of (a)Down-facing surface of part manufactured with VED of 13.07 J/mm^3, (b) Down-facing surface of part manufactured with VED of 39.22 J/mm^3, (c) Down-facing surface of part manufactured with VED of 166.67 J/mm^3.

in the figure. On the other hand at locations where the melt does penetrate minimally, right before the meltpool solidifies, due to the high surface tension of molten metal, the tip of the meltpool starts to spread on top of nearby powder particles, instead of penetrating further through the powder bed. The powder particles are then sintered to this spreading meltpool creating an artefact that resembles an 'inverted mushroom' like structure. These artefacts, together with the areas of insufficient penetration create large valleys and peaks within the surface which creates the high surface roughness as measured and shown on Figs. 9 and 10.

Fig. 11 (b) depicts a more uniform surface with occasional pits, however with an almost complete coverage of powder particles attached to the surface as is the norm for down-facing surfaces. This particular sample had only minimal dimensional deviation and is thereby as close to optimal as possible while still maintaining a relatively low *Sq* value.

Fig. 11 (c) shows a surface that is completely covered by partially melted powder. Due to the high VED exerted on the powder, this results in the formation of a melt pool with increased dimensions of length, width and depth [22]. Additionally due to the high melt pool temperature, the melt viscosity is also reduced which results in the formation of a highly flowable melt. Literature also suggests that at high VED the melt pool transitions to a keyhole mode where the direction of the melt flow is downwards directly into the powder bed, towards the printing platform [16,41]. The Keyhole mode is especially likely as the VED is very high in this region and the scanning is taking place in a region where the start and end point of the scan tracks are especially close together, facilitating the formation of a large heat affected zone and deep melt pool. Therefore this highly flowable meltpool, due to its large wettability is able to flow into the powder bed, either fully or partially melting any adjacent powder particles that the melt comes in contact with. Due to the instability of the melt in the dross region it can also be assumed that the dross formed is accompanied by various pores, keyhole pores, lack-of-fusion defects [22]. Similar to what was described in the low VED condition, in the current case, the downward flowing meltpool, as its temperature reduces and its viscosity increases, as the meltpool begins to solidify, the high surface tension of molten metal causes it to spread on top of powder particles, thereby halting the penetration. However, in this case the meltpool is much larger as the meltpool spreads on top of powder, once again particles are melted or attached to the meltpool causing the formation of large, uniform and smooth dross as seen in Fig. 11 (c), which is indicative of the very low *Sq* value of the surface as can be seen in graphs in Figs. 9 and 10.

3.2. *Down-facing surfaces of 35°*

For the 35° down-facing surface as well, graphs investigating the relationship and trends between VED, *Sq* and relative dimensional error are displayed in Figs. 12 and 13. The *Sq* and the relative dimensional error are fit with trend lines with logarithmic fits while the VED is depicted on the 'X' axis.

Observing the graphs in Fig. 12 and 13, the indications for the 35°overhangs are similar to those of the 45°. It becomes evident that for both the 60 μm and 90 μm layer thickness processes, the relative dimensional error increases with an increase in VED. While for surface roughness, for both 60 μm and 90 μm layer thickness the surface roughness decreases while increasing the VED with the minimal *Sq* being measured at the highest VED. The reason for which is the same as already discussed with the 45° samples. For the 60 μm and 90 μm layer thickness, a region of around 35–60 J/mm^3 VED (for 60 μm LT) and ~~35~~ 20 – 40 J/mm^3 (for 90 μm LT) are suggested as optimal processing windows where the surface roughness are still low while maintaining a dimensional error below 20% which can be compensated with relative ease during the design creation phase.

Fig. 14 (a) depicts the down-facing surface of samples produced with the lowest VED, for the 60 μm LT and the 90 μm LT. The resultant surface is similar to the lowest VED surface for the 45° samples, and the mechanism of the surface formation is similar. The VED applied by the laser is low which results a smaller meltpool resulting in a smaller heat affected zone resulting in minimal penetration of the meltpool into the powder bed, which causes the part to be smaller than the intended design. This in combination with the hydrodynamic instability of the melt driven by the Marangoni effect, and the formation of 'inverted

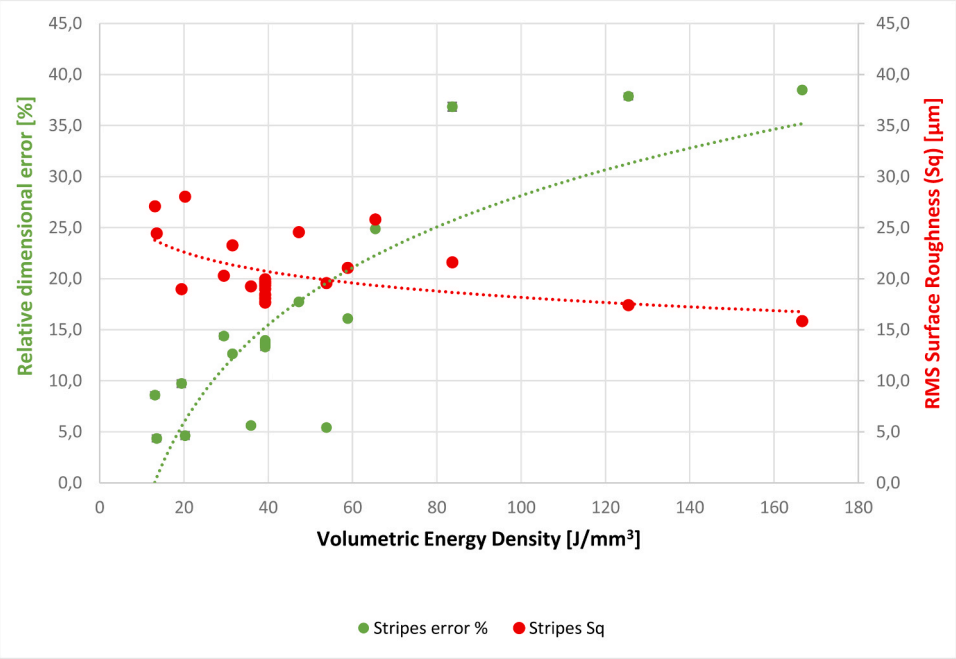

Fig. 12. Trends between relative dimensional error, Sq and VED for 35° samples with 60 µm layer thickness.

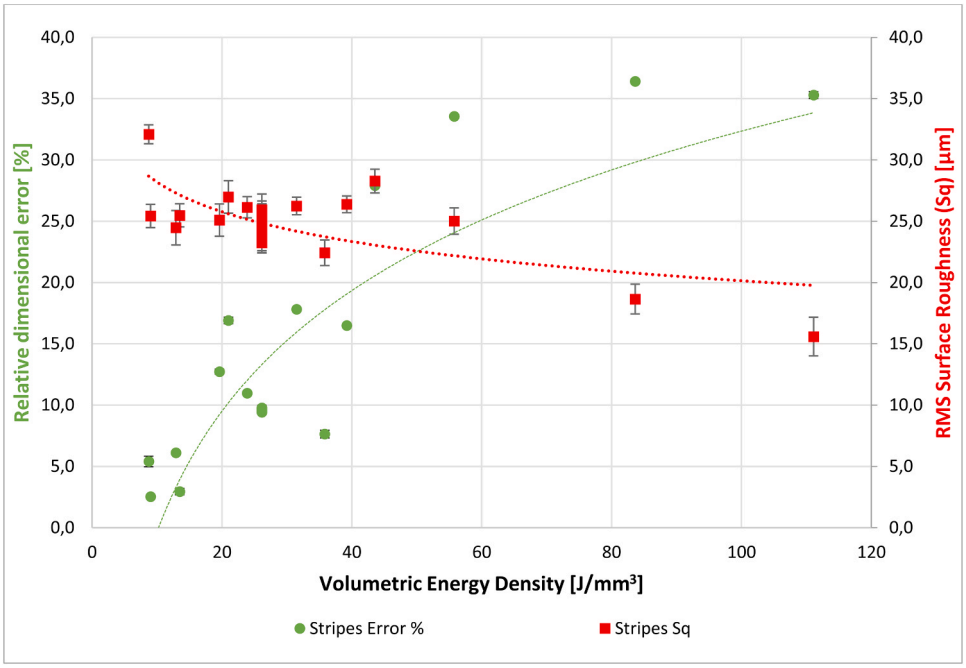

Fig. 13. Trends between relative dimensional error, Sq and VED for 35° samples with 90 µm layer thickness.

mushroom' artefacts, as explained in the previous section creates the large valleys and peaks within the surface which creates the high surface roughness as measured.

Fig. 14 (b) depicts the surface of the 35° samples that represents a stable working area for printing 35° overhang surfaces. As in both the cases of 60 µm LT and 90 µm LT, the measured values of the *Sq* reduced, while the relative dimensional error is measured to have reduced as well. Both these surfaces are characterised by a uniform surface with occasional pits, however with an almost complete coverage of powder particles attached to the surface. While, Fig. 14 (c) depicts, similar to the high VED surface of the 45° surface, a surface that is completely covered by partially melted powder. These surfaces similarly also revealed low *Sq* while showing very high relative dimensional error because of the large dross formations. The reason for this is the same as the discussion held for the 45° surface.

3.3. *Down-facing surfaces of 25°*

Graphs investigating the relationship and trends between VED, *Sq* and relative dimensional error for the 25° down-facing surface are displayed in Figs. 15 and 16. The *Sq* and the relative dimensional error are fit with trend lines with logarithmic fits, while the VED is plotted on the

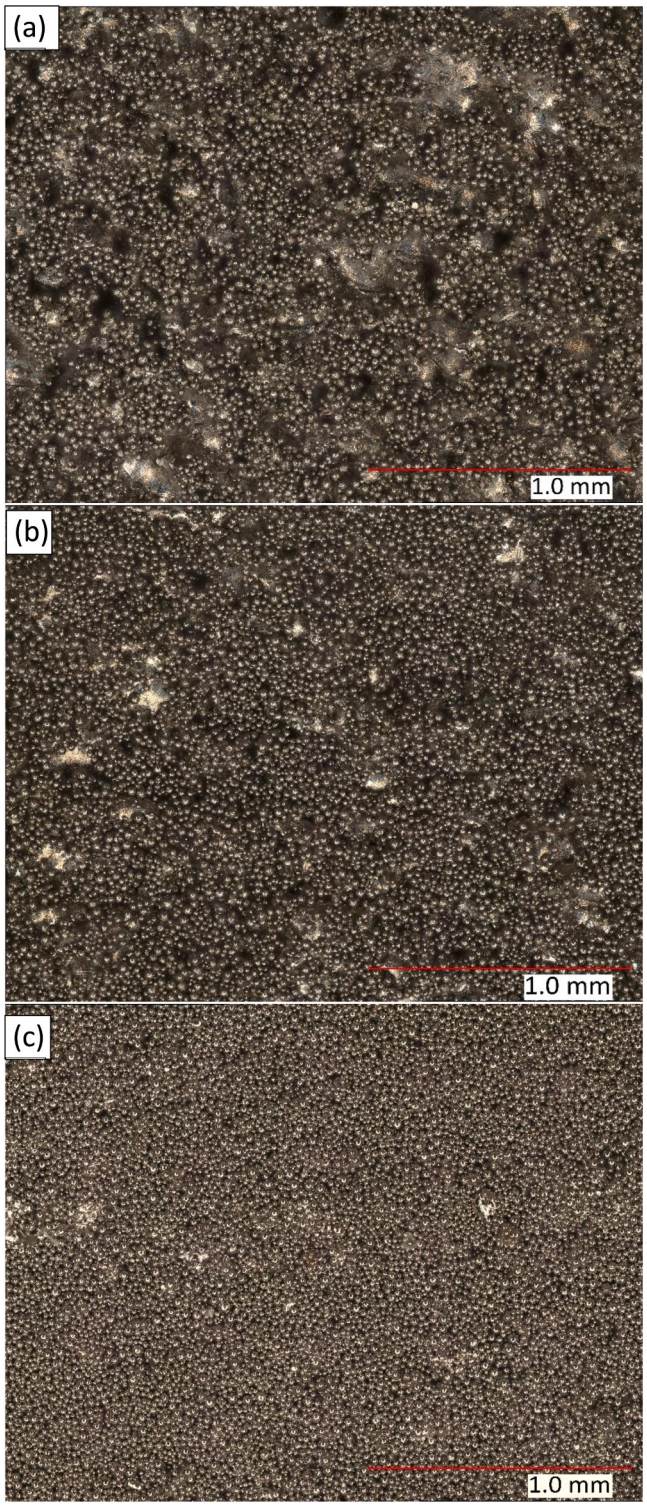

Fig. 14. Top view (Surface plane) of Down-facing surfaces produced with VED of (a) 9 J/mm^3, (b) 35.8 J/mm^3, and (c) 111.11 J/mm^3.

'X' axis.

Observing the graphs in Figs. 15 and 16, similarities between the previously seen 35° and 45° overhangs remain. It becomes evident that for both the 60 μm and 90 μm layer thickness processes, the relative dimensional error increases with an increase in VED. This trend is almost identical to what is seen for the 35° and 45° down-facing surface. For both the 60 μm LT and 90 μm LT samples, the trend of *Sq* increases with an increase in VED. For the 60 μm and 90 μm layer thickness, a region of around 35 – 60 J/mm^3 VED (for 60 μm LT) and 20 – 40 J/mm^3 (for 90 μm LT) is suggested, which would represent regions where the relative dimensional error is at its least while the *Sq* is also at the least and therefore they are an indication as to an optimal process window for the printing of low surface roughness, low relative dimensional error at 25°overhangs surfaces.

Fig. 17 depicts the down-facing surface of 25° overhang samples.

Fig. 17 (a) depicts a very similar surface to the low VED surfaces of 45° and 35° overhangs and these depict surfaces that are now typical for a surface produced with low VED. The measured value of the *Sq* is higher than for the 45° and the 35° surface due to the nature of 25° angle having even lesser capacity for heat transfer away from the part. However, with the low VED, the meltpools are not able to penetrate into the powder bed, which results in large negative relative dimensional error (part smaller than intended) especially for the 90 μm LT. The large pits and peaks formed as a result of this as well as the 'inverted mushroom' artefacts contributes towards the high measured *Sq*.

Fig. 17 (b) depicts the surface during the 'optimal' processing condition. 'Optimal' because they depict the situation when the dimensional deviation is minimal at the low *Sq* values. However, when comparing with optimal surfaces of other angles, the *Sq* is higher, which is explained by the lower attempted angle of printing 25°. In this region of VED, the meltpool begins to penetrate deeper into the powder bed in keyhole mode, causing large deep heat affected zones. Dross formation begins to manifest. But the surface is highly irregular as the VED is only high enough to create melt that flows into the powder bed, this is why the surface also has high *Sq*.

Fig. 17 (c) depict a surface that is typical for a surface produced with extremely high VED. The melt mechanism is the same as what happens with the 45° and 35° surfaces, thereby causing the smooth surface, with very high relative dimensional error. For the respective mechanisms, the reader is referred to the 45° section.

3.4. Statistical analysis

The processing and statistical analysis of the above acquired data is then accomplished using MATLAB (R2019a) to generate the predictive process equations that could describe the relationships between the different process parameters and the process responses, while different models are built for the 2 different layer thicknesses.

In the following section regression-based equations for the 45° inclined angle for the responses of dimensional error % and *Sq* are presented. The equations for the investigated 35° and 25° are further given in Appendix A. The methodology for the generation and fitting of the model for the various angles are identical.

A number of different common regression formulae are identified and the equation that has the best fit to the experimental data is chosen as the preferred equation, in order to maximize the probability of accurate predictions. A quadratic regression method is used to fit the second-order polynomial seen in Eq. (2) to the measured experimental data:

$$y = b_0 + \sum b_i x_i + \sum b_{ii} x_{ii}^2 + \sum b_{ij} x_i x_j \quad (2)$$

In this equation, y represents the desired output variable, which in this case are the relative dimensional error and *Sq* respectively, while b_0, bi, b_{ii}, and b_{jj} are the regression coefficients or predictors; and x_i is the value of the ith factor.

Of the four process parameters, laser power, scan speed and scan spacing are input as quantitative process parameters and scan pattern is input as a categorical (qualitative) process parameter so as to reflect reality. The developed equations resulting from the quadratic regression formulation with the best fits – for the four process parameters that are studied in this work – and the values generated for the coefficient of each significant process parameter presented in Eq. (2) where:

x_1 is the laser power, x_2 is the scan speed, and x_3 is the scan spacing.

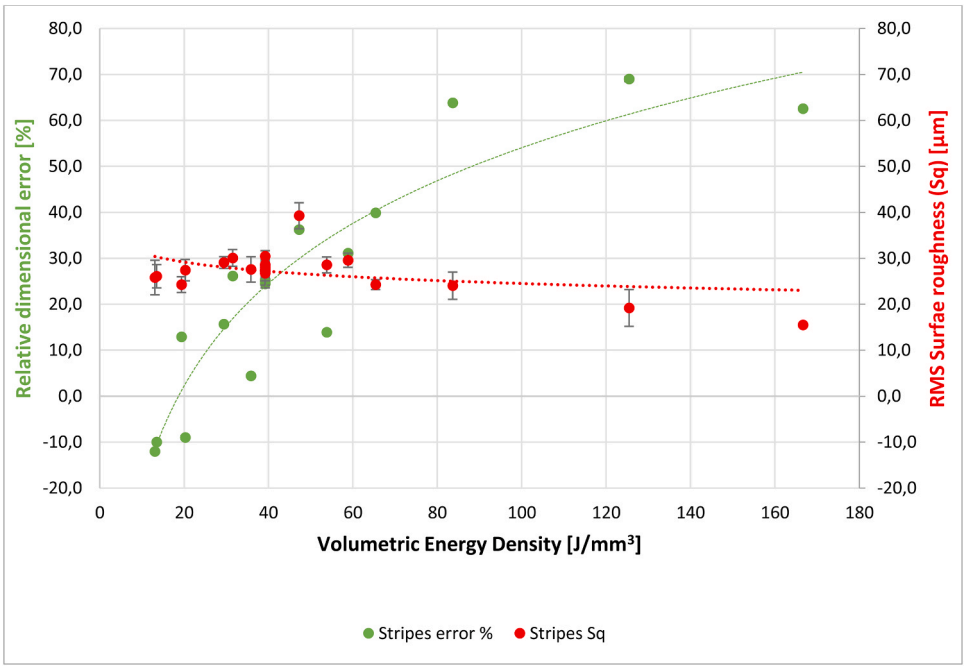

Fig. 15. Trends between relative dimensional error, Sq and VED for 25° samples with 60 µm layer thickness.

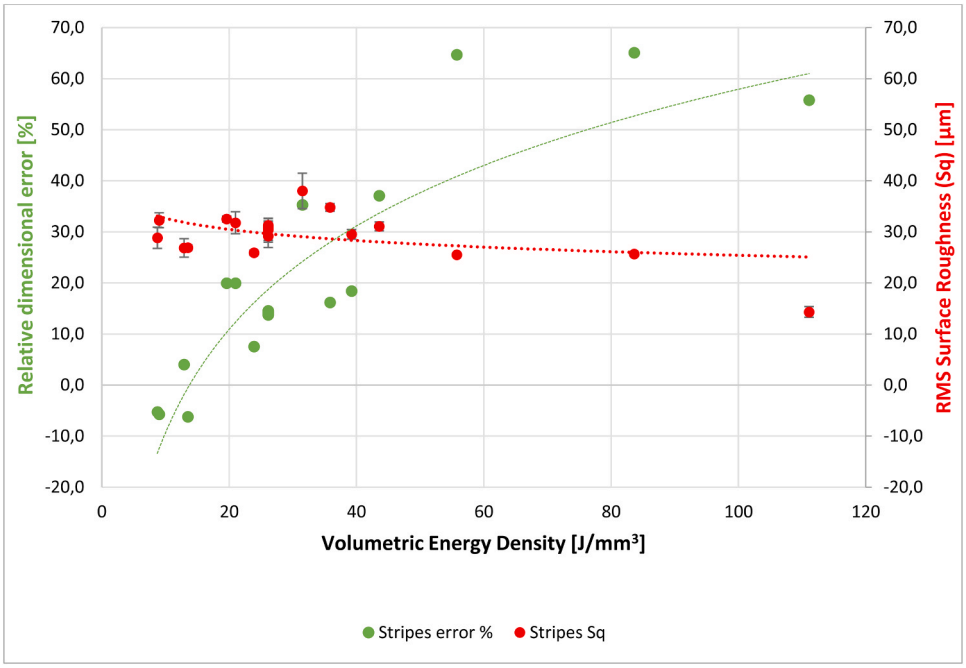

Fig. 16. Trends between relative dimensional error, Sq and VED for 25° samples with 90 µm layer thickness.

The developed equations for the 45° down-facing surface are seen below. The range of the values that can be used for prediction by the equations can be seen in Table 3.

3.5. Regression equations for dimensional error %

For 60 µm Layer thickness;

$$Rel.\ Dim.\ Err. = -6.25 + 0.21LP - 0.012SS - 10.21e^{-5}LPSS + 1.17e^{-5}SS^2 \quad (3)$$

R-squared: 94.9%.

For 90 µm Layer thickness;

$$Rel.\ Dim.\ Err. = -29.15 + 0.27LP - 0.028SS + 0.81SG + 4.90e^{-5}LPSS - 0.0028LPSG + 8.017e^{-6}SS^2 - 0.0032SG^2 \quad (4)$$

R-squared: 93.9%.

3.6. Regression equations for Sq

For 60 µm Layer Thickness;

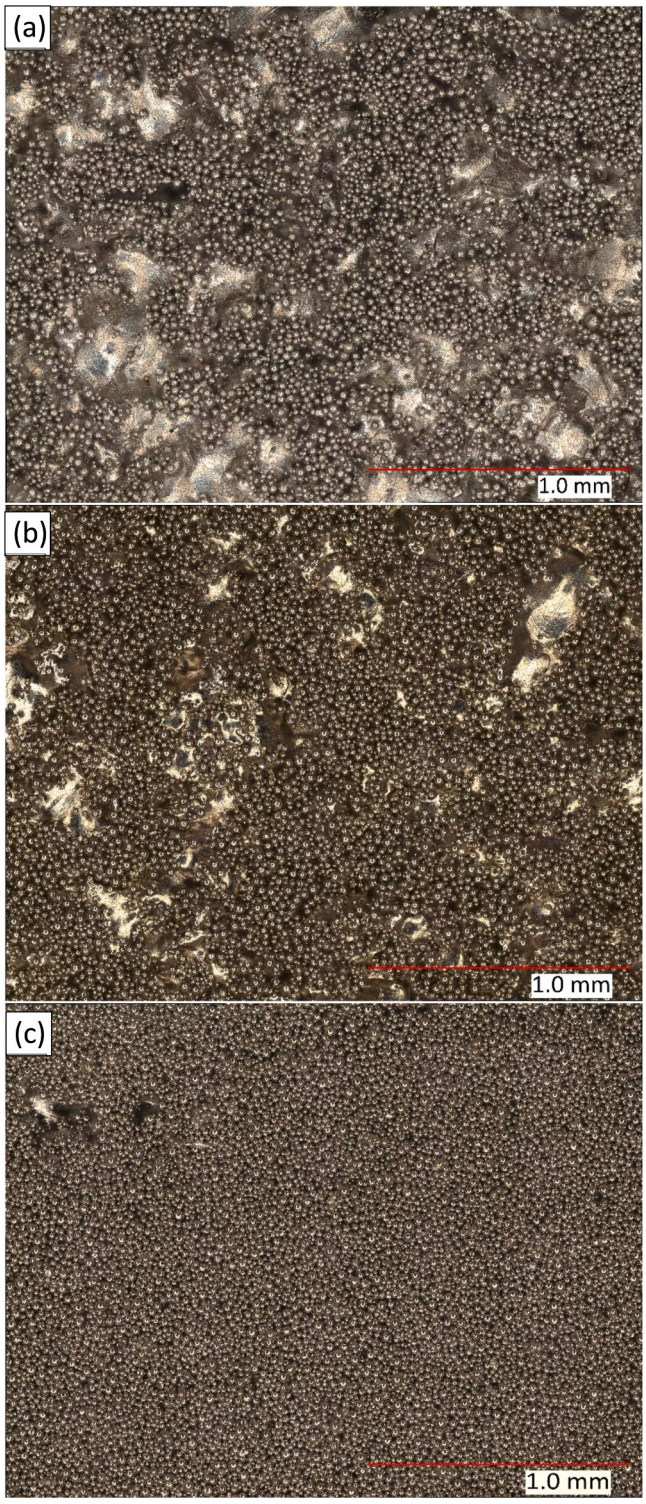

Fig. 17. Down-facing surfaces produced with VED of (a) 9 J/mm^3, (b) 23 J/mm^3 and (c) 111.11 J/mm^3.

$$Sq = 22.55 - 0.17LP + 0.015SS - 4.81e^{-5}LPSS + 6.94e^{-4}LP^2 - 2.76e^{-6}SS^2 \quad (5)$$

R-squared: 80.1%.

For 90 μm Layer Thickness;

$$Sq = 33.71 - 0.24LP + 0.021SS + 8.17e^{-4}LP^2 - 7.59e^{-6}SS^2 \quad (6)$$

R-squared: 82.1%.

Table 3
The range of different process parameters to be used for prediction.

Process Parameter	Range
Laser Power (LP) [W]	50–250
Scan Speed (SS) [mm/s]	200–1500
Scan Spacing (SG) [μm]	50–100
Scan Pattern (SP)	Stripes
	Rectangular cell
	Hexagonal cell

An analysis of variance (ANOVA) is conducted and based on the results, the equations presented above only contain the parameters that are found to have a significant effect on the dimensional accuracy and surface roughness of down-facing parts. Main effect and interaction effects of parameters that had high p-values (p-value > 0.05) are considered insignificant and discarded from the process model as their effects in this case can be considered to be negligible noise. The ANOVA analysis also confirms the most significant individual process parameters. For 60 μm LT, for the dimensional accuracy in 45° down-facing surfaces the interaction effect of Laser power and Scan speed is the most significant (p-value $\approx 8.89 \times 10^{-10}$) while for surface roughness, the second order effect of laser power is the most significant (p-value $\approx 8.79 \times 10^{-16}$). While for 90 μm LT, for the dimensional accuracy the laser power is the most significant parameter (p-value $\approx 1.82 \times 10^{-8}$) and for surface roughness the second order effect of laser power is the most significant (p-value $\approx 8 \times 10^{-20}$). This is in agreement with previous works where laser power and scan speed are prominently visible in the equations, which can be explained since together they form the basic blocks of energy density that is applied on the powder by the laser; energy density being one of the main aspects that govern the meltpool characteristics as discussed in the previous sections.

Furthermore, these equations prove one of our initial assumptions as discussed in the beginning of Section 3: the effect of scan pattern within the down-facing area is minimal. These equations are in agreement with this hypothesis as scan pattern data which was input as a categorical parameter during the modelling process is not present in any of the equations due to having very high p-values and therefore minimal significance on the overall process. Therefore the equations above can be used to predict dimensional accuracy and *Sq* within down-facing surfaces, irrespective of what scan pattern is chosen, since the final output will remain the same for all purposes.

The reason for this is that the effective cross sectional area of the down-facing region, where the process parameters are varied, is not large enough for scan pattern to have a significant effect, unlike other process parameters such as laser power, scan speed and scan spacing. Another interesting observation from the equations is that scan spacing is not considered a significant enough parameter to affect dimensional accuracy and surface roughness of 60 μm layer thickness parts, however is found significant for the 90 μm layer thickness samples.

The built models for the 35° and 25° down-facing surfaces are shown in Appendix A, Eq. A.1–Eq. A.8. It is to be noted that the Eqs. (3), (4), (5), and (6) are valid for the investigated material (Ti6Al4V) for the LPBF system ProX DMP 320. However, the optimums as well as the equations can be considered to be significant for other similar Titanium based alloys that are printed through other LPBF systems. For this purpose, further validation is therefore also warranted. The authors do not guarantee the validity of the equations for other materials producible by LPBF systems such as other Nickel based alloys or Steel based alloys. Therefore, this is a limitation that is imposed on the equations considering the material and machine studied.

Additionally, since productivity is one of the foremost drivers for parameter selection, the easiest way to include productivity when also improving the surface quality and dimensional accuracy of a part, is through choosing the highest values for layer thickness, hatch spacing and scan speed. Productivity is directly proportional to all of these

quantities. Therefore, since various parameter conditions might provide parts of a similar quality, it is favourable to choose the working parameter based on the logic just mentioned. Keeping this in mind, optimized process parameters can be suggested.

At 60 μm layer thickness: laser power of 150 W, scan speed of 850 mm/s and scan spacing – 75 μm, while laser power of 190 W, scan speed of 800 mm/s and 75 μm scan spacing is recommended for 90 μm layer thickness.

3.7. Validation

Following up on the observations made in the previous section and the developed quadratic equations, further test pieces are printed in order to experimentally validate the accuracy of prediction of the developed equations. The planned experimental design varied the VED of the printing process from very low VED until extremely high VED. This is intended to observe the print at a wider range of VED. A common scanning strategy called 'Stripes' is chosen and two batches are printed for each layer thickness, again in order to observe the repeatability of the process performance. A total of 18 samples are printed within each batch and Table 4 shows the process parameters for samples printed at both 60 μm and 90 μm layer thicknesses.

In order to test the accuracy of the equations, of the 18 printed test pieces, samples 1,2,5,7, 10, 16 and 17 have parameters that were previously used in printing in the experimental phase, samples 3,4,9, 12, 13, 14, 15 and 18 represent new parameter combinations. However, samples 6, 8 and 11 are printed using parameters that are outside the range of the previous experimental phase.

The whole experimental results of the printing as well as the prediction based on the equations can be seen in the Table A. 1 and Table A. 2 in Appendix A. The following observations and inferences are made based on the measurements and predictions.

3.7.1. Predictability of different angles

The quadratic equations provide better accurate predictions for the overhang angles of 45° and 35°, while the predictions of the 25° overhang surfaces is poorer. Of the 18 samples in both batches, applying a tolerance limit of 5 μm for *Sq* and 5% for relative dimensional error of the 60 μm layer thickness samples and a 10 μm and 10% tolerance limit for the *Sq* and relative dimensional error of the 90 μm layer thickness samples, the accuracy of prediction can be seen in Table 5.

3.7.2. Predictability and optimal printing zones

The accuracy of the prediction in the optimal printed zones as suggested in the previous section is good. This observation leads to the conclusion that at these optimal conditions the process itself is more stable and thus contributing towards an improved predictability as seen in Table 6.

Table 4
The experimental design for the validation.

Part number	laser Power [W]	Scan Speed [mm/s]	Scan Spacing [μm]	VED for 60 μm LT [J/mm^3]	VED for 90 μm LT [J/mm^3]
1	90	1235	60	20.24	13.50
2	150	1500	75	22.22	14.81
3	100	780	90	23.74	18.99
4	140	1000	75	31.11	20.74
5	210	1235	90	31.49	20.99
6	300	1750	90	31.75	21.16
7	150	850	75	39.22	26.14
8	45	180	90	46.30	30.86
9	190	800	75	52.78	35.19
10	90	465	60	53.76	35.84
11	320	1600	50	66.67	44.44
12	200	500	90	74.07	49.38
13	75	150	90	92.59	61.73
14	175	390	60	124.64	83.10
15	250	370	90	125.13	83.42
16	210	465	60	125.45	83.63
17	150	200	75	166.67	111.11
18	250	330	60	210.44	140.29

Table 5
Predictive accuracy of different angles.

Layer Thickness	Angle	No. of samples within tolerance limit for *Sq*	No of samples within tolerance limits for Error %
60 μm	45°	18	15
	35°	16	11
	25°	11	6
90 μm	45°	14	14
	35°	11	14
	25°	18	6

4. Discussion

The results as shown in the previous section above allow the characterization of down-facing surfaces in three broad categories distinguished as a result of three different printing conditions. Namely the 'Low VED', 'Optimal VED' and 'High VED' down-facing surface. The following discussion section will investigate the mechanism of formation of these different surfaces, their characteristics and the reason for this behavior.

4.1. Surface formation in down-facing features

4.1.1. a. Low VED printing

Low VED surfaces are characterized by their low relative dimensional error and high surface roughness. In fact, many surfaces formed by low VED printing results in parts that are smaller than the intended design. Fig. 18 depicts a surface texture map of a highly irregular surface characterized by small irregular pits and protrusions seen as bright blue and red spots. This irregularity is caused by insufficient penetration of the meltpool at certain locations and minimal penetration at other locations. This irregular surface is the reason the low VED surfaces have high surface roughness. The randomly distributed minute red spots seen in Fig. 18 depict the protrusions from the surface that are further discussed in the following section. The legend of the texture map also confirms the large range of height variation within the surface. The surface displays a variation of over 500 μm from the blue points that depict deep pits within the surface and the red spots which depict tall protrusions on the surface caused by the deep vertical penetration of the meltpool causing the described 'inverted mushroom' artefacts.

The SEM micrograph in Fig. 19 (a) show minute inverted 'mushroom' like structures. It is postulated that these minute features are caused by the localized seepage of the meltpool slightly into the powder bed (about 100 μm) in the extremes of the scan vectors, where there is a chance of the formation of an overheated zone. However, as the inherent VED is quite low, the meltpool does not flow a great distance, and only manages to partially melt powder particles around them causing the formation of the inverse 'mushroom' structures. As discussed in earlier sections, as the meltpool begins to cool down, its viscosity increases and

Table 6
Predictive accuracy in the optimal printing zone.

Layer Thickness	Angle	Optimal zone [J/mm^3]	Sample	*Sq* Error [μm]	Relative Dimensional Error [%]
60 μm	45°	30 – 50	7	-0.76	-2.71
	35°	35 – 60	10	3.47	-5.64
	25°	35 – 60	10	3.95	-2.47
90 μm	45°	30 – 50	9	5.23	0.18
	35°	20 – 40	10	-4.48	1.08
	25°	20 – 40	10	0.29	0.15

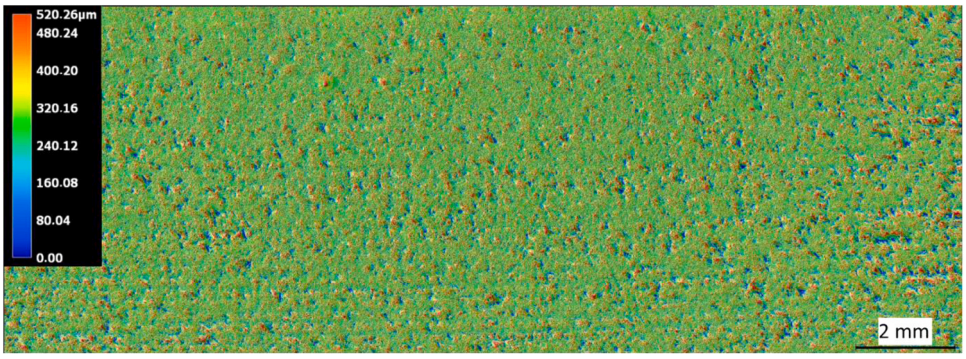

Fig. 18. Surface texture map of low VED down-facing surface.

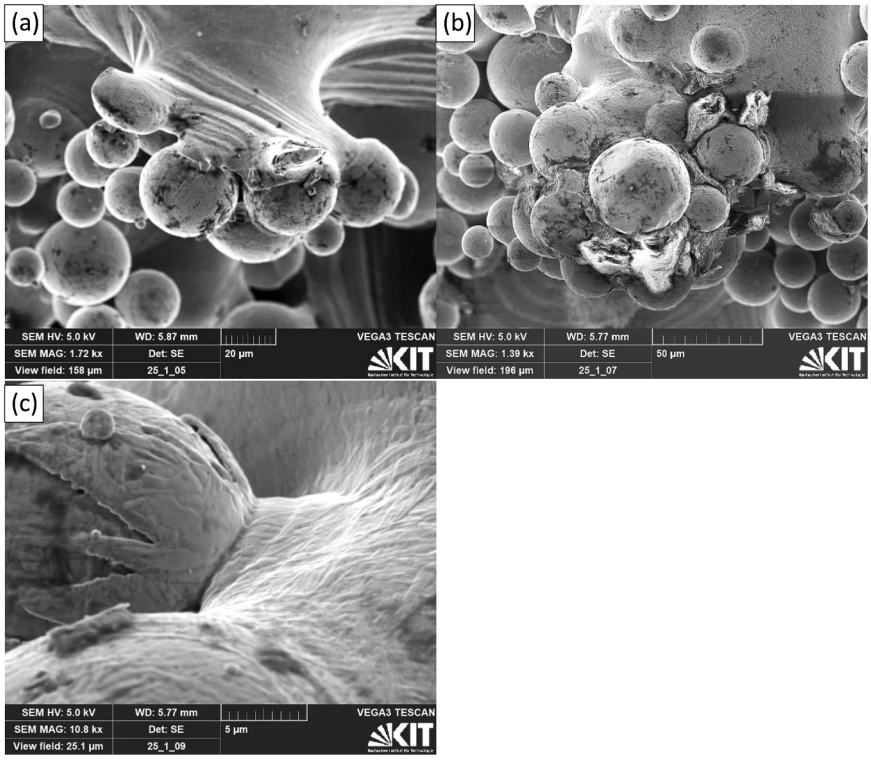

Fig. 19. SEM micrograph of low VED down-facing surfaces (a) showing the side view of inverse mushroom like structures causing high surface roughness,(b) top view (surface plane) of irregular dross formations with partially melted powder causing deep protrusions and (c) a powder particle attached to the meltpool flowing in its surroundings.

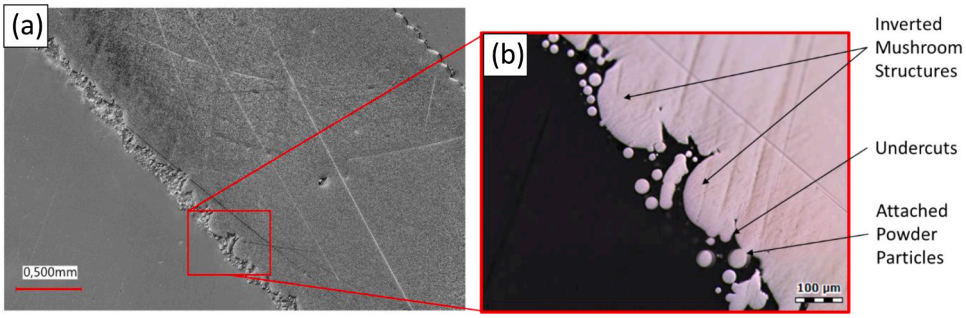

Fig. 20. Optical Microscopy image of cross cut of low VED down-facing surface (a) overview of polished cross section and (b) the detailed surface morphology and defects.

due to its high surface tension, it begins to widen and spread on top of powder particles. Thereby attaching nearby powder particles onto itself as seen in Fig. 19 (b) and (c), creating the inverted 'mushroom'-like structures. Naturally, these inverse 'mushroom' structures that have formed are the reason for the very high surface roughness measured in the low VED surfaces. Fig. 20 (a) depicts the polished cross section of the down-facing area where in Fig. 20 (b) the inverted mushroom like structures and partially melted powder particles are visible. It is seen that these features which cause the high surface roughness, also result in the formation of undercuts and surface irregularity, which can increase the potential for micro-crack propagation. It is also worth mentioning that such near-surface defects clearly show the difficulty in comprehensively characterising surface texture.

4.1.2. b. High VED printing

The high VED surface shows high dimensional deviation and low surface roughness. Fig. 21 depicts a surfaces that is irregular and formed as a result of high VED. Furthermore, the surface also shows the formation of longer macro size 'ranges' of groups of hilly structures. The surface is characterized by large flat areas (seen in blue) and in certain areas deep protrusions into the powder bed as seen as the red spots on the texture map in Fig. 21.

Fig. 22 (a) depicts one large smooth melt lake, formed as a result of the high VED input and is formed, as the meltpool flows directly into the powder and it has a large depth, length and width [22]. However, when the meltpool begins to cool down, its viscosity decreases, and combined with a high surface tension, the meltpool cannot flow into the powder anymore and in turn flows flatly on top of powder, causing these large flat spots within the surface. These flat spots can also combine with other adjacent melt pools, resulting in large uniform dross formations that show low surface roughness as seen in Fig. 22 (d). Fig. 22 (d) shows this phenomenon in more detail where adjacent layers can be seen to be merging into flat surfaces due to the increased penetration and the subsequent spreading and solidification of the melt.

Fig. 22 (b) and (c) depict the large deep penetrations of the meltpool directly into the powder bed. It is postulated that these structures are formed as a result of keyhole mode of printing in this particular region caused at a point such as the end of a scan vector. This keyhole mode is known to cause various very deep and narrow/slender melt pools. Furthermore, the keyhole mode of printing also causes the formation of porosity, which can be seen in Fig. 23 (a) and (b) where the cross section is shown to have an increased prevalence of near-surface porosity. Fig. 23 (b) also shows that when compared to the low VED printing mode, there is an absence of inverted mushroom like structures and instead the surface is smoother, albeit with powder particles attached.

4.1.3. c. Optimal VED printing

Similar to all down-facing surfaces, powder particles are attached to the surface as can be seen in Fig. 24 and Fig. 26. This is unavoidable as the meltpools formed always come into contact with the loose powder of the powder bed. The presence of deep pits and peaks is reduced, and the surface shows slightly more regularity in comparison with the low VED surface though higher and lower areas exist. However, the height range within which the surface varies is significantly smaller than in the other 2 conditions. The inverse 'mushroom' structures are not present in this surface which explains the lower surface roughness, however, smaller protrusions into the surface do exist as seen in Fig. 25 (b). The cross cut in Fig. 26 (b) confirms that in an optimal printing mode, the surface is seen to be largely smoother at many locations and with the occasional presence of attached powder particles and near surface porosity. There is a notable absence of inverse mushroom structures as well as near-surface defects such as undercuts and surface irregularities as can be seen in the low VED conditions and a reduced presence of near-surface porosity when compared to the high VED conditions.

4.1.4. d. Process stability window

To summarize the results from the conducted experiments, the following process stability window is presented in Table 7, which denotes the optimal VED to be used within the down-facing area of Ti6Al4V components produced by laser powder bed fusion for various angles and layer thicknesses. Down-facing surfaces remain sensitive features and this table can act as a starting point for attaining stable qualities..

5. Conclusion

The present research work provides an in-depth analysis on the underlying mechanism of printing in the down-facing region of metal parts produced by L-PBF processes. By doing so it fills an existing gap in a topic within metal AM that is so far still in the beginning of exploration. Furthermore, the present work also increases the overall process knowledge in the LPBF process. The conclusions can be summed up in the following points.

- It is found that the initial assumption that volumetric energy density could be a significant process parameter to characterise down-facing surfaces is correct, due to the variations in meltpool dimensions as a result of volumetric energy density.
- VED can be used as it gives an indication on the degree of overheating within the down-facing area which directly relates to dross formation.
- For all three different down-facing angles, the behaviour of dimensional deviation increases with increased VED and surface roughness reduces with increased VED.
- Within the 'Low VED' mode, the 'inverse mushroom' like artefacts are formed as the meltpool starts to solidify, which causes the high surface roughness. While for the 'High VED' mode this effect happens on a larger scale, which results in nearby meltpools attaching to each other leading to large flat surfaces, which cause the low surface roughness.

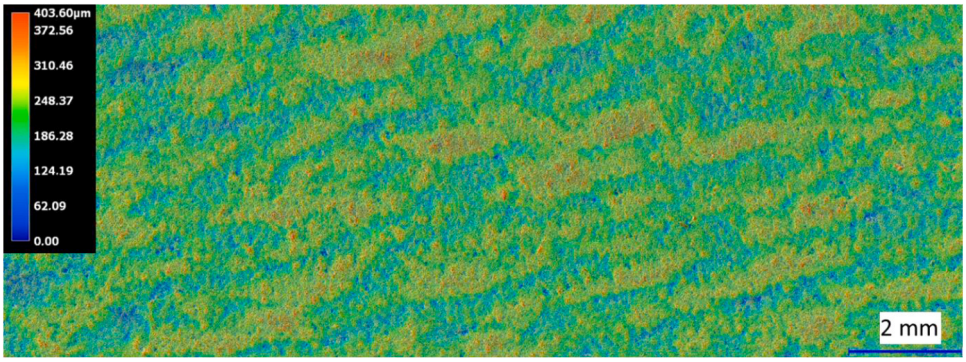

Fig. 21. (a) Surface texture map of a high VED down-facing surface.

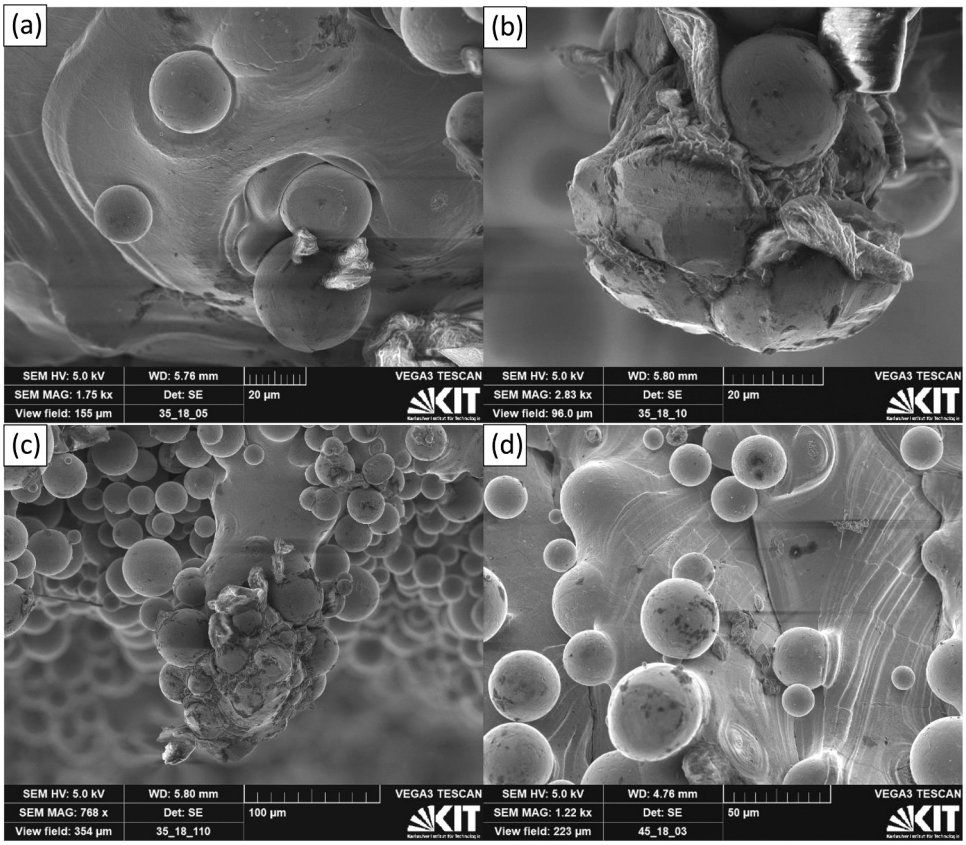

Fig. 22. SEM micrograph of a high VED surface with (a) a top view (surface plane) of a large melt lake formations and (b) and (c) depict the large deep seepage of meltpools into the powder bed, (d) shows the top view of flat surfaces caused by overlapping adjacent meltpools from successive layers.

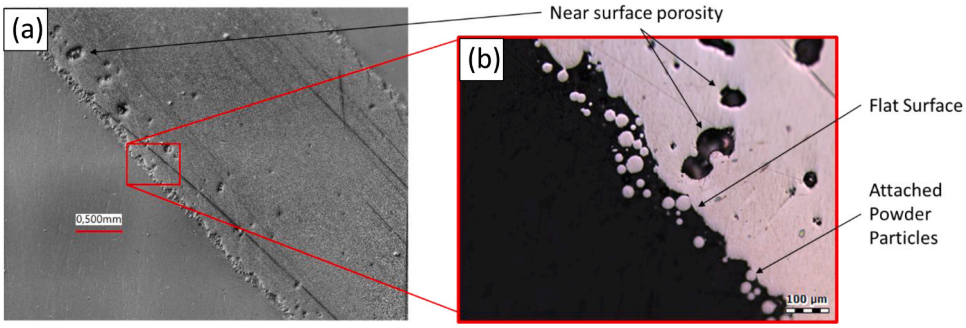

Fig. 23. Optical Microscopy image of cross cut of high VED down-facing surface (a) overview of polished cross section and (b) the detailed surface morphology and defects.

- At the 'Optimal VED' condition the surface does display coverage of powder particles which are sintered to the surface; this is unavoidable for the as-built condition of down-facing surfaces.
- The cross cuts further show that the near-surface porosity increases as a function of the energy density applied. Additionally, it is seen that the inverted mushroom features that cause the high surface roughness of 'Low VED' down-facing surfaces, also introduce undercuts, that further increase the difficulty of optical surface characterisation. Therefore, it is recommended to combine surface roughness values with characterisation methods for surface and near-surface defects such as porosity etc, that might better reflect the criticality of down-facing surfaces.
- The present paper also establishes predictive equations based on a Design of Experiments study that can be used in order to predict quality marks, within down-facing areas of Ti6Al4V alloy, where laser power and scan speed are confirmed as the most significant process parameters.
- When a number of good parameter sets can be chosen as per the developed equations, it is preferable to choose one that maximises the productivity of the process by choosing the highest layer thickness, hatch spacing and scan speed when possible. Especially in an industrial context this is vital for the fast adoption of metal AM technologies.

Future work will focus on continually improving the developed regression models with the inclusion of further process parameters as well as the establishment of a unified process model for the prediction of quality marks for any down-facing angle, as required by the designer. The developed equations will be used in the future to predict/optimise complex features/surfaces for practical engineering applications.

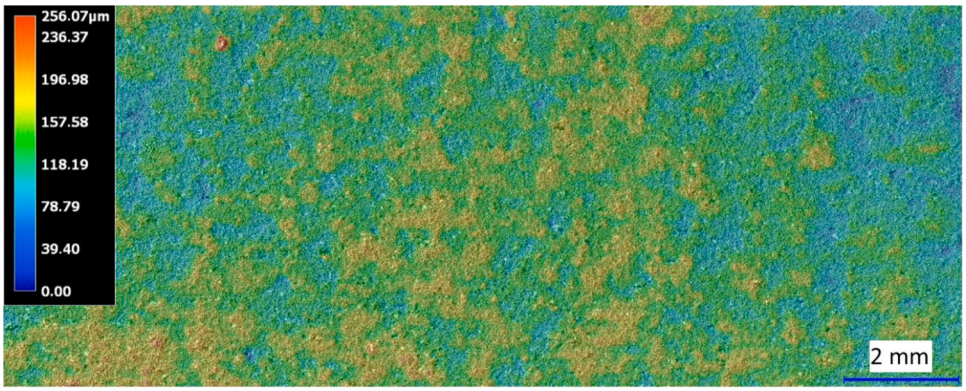

Fig. 24. Surface texture map of an optimal VED down-facing surface taken with a top view of the surface.

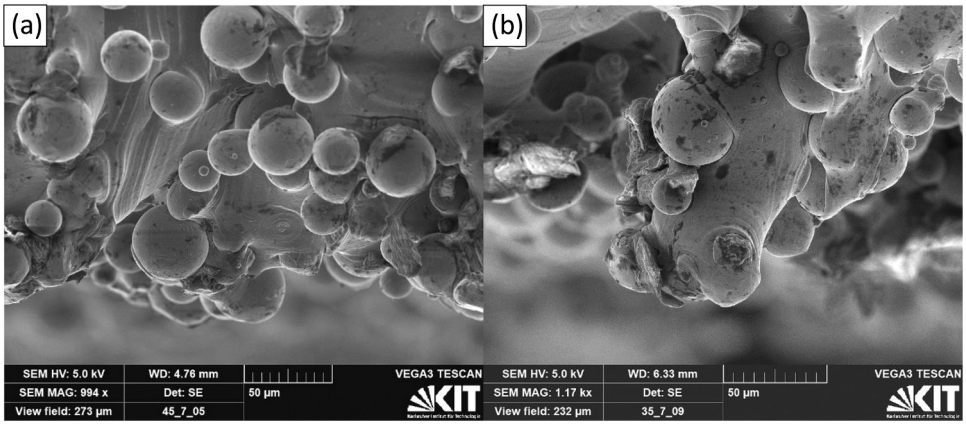

Fig. 25. Side view (a) SEM micrograph of an optimal VED down-facing surface and (b) smaller protrusions into the surface still exist.

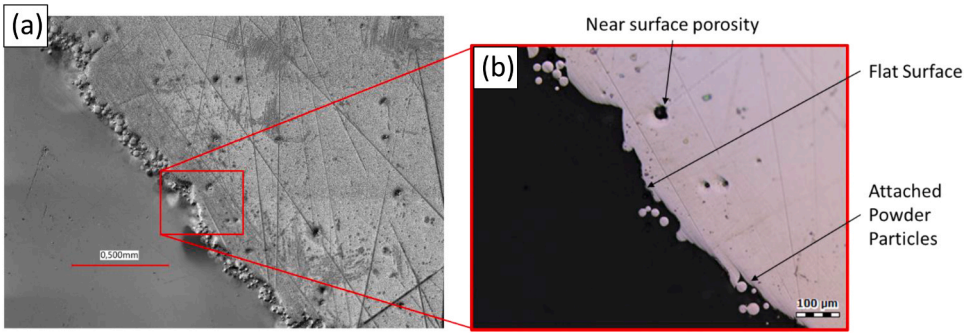

Fig. 26. Optical Microscopy image of cross cut of low VED down-facing surface (a) overview of polished cross section and (b) the detailed surface morphology and defects.

Table 7
Process Stability window depicting low, optimal and high VED conditions for the different layer thicknesses and overhang angles.

Layer Thickness [µm]	Angle	Low VED [J/mm^3]	Optimal VED [J/mm^3]	High VED [J/mm^3]
60	45°	< 30	30 – 50	> 50
	35°	< 35	35 – 60	> 60
	25°	< 35	35 – 60	> 60
90	45°	< 30	30 – 50	> 50
	35°	< 20	20 – 40	> 40
	25°	< 20	20 – 40	> 40

CRediT authorship contribution statement

Amal Charles: Methodology, Software, Validation, Formal analysis, Investigation, Data curation, Writing - original draft, Visualization. **Ahmed Elkaseer**: Software, Validation, Formal Analysis, Writing - review & editing. **Umberto Paggi**: Software, Validation, Investigation. **Lore Thijs**: Conceptualization, Investigation, Resources, Writing - review & editing, Supervision, Project administration, Funding acquisition. **Veit Hagenmeyer**: Writing - review & editing, Supervision. **Steffen Scholz**: Methodology, Formal Analysis, Resources, Writing - review & editing, Visualization, Supervision, Project administration, Funding acquisition.

Declaration of Competing Interest

The authors declare that they have no known competing financial interests or personal relationships that could have appeared to influence the work reported in this paper.

Acknowledgements

This work was conducted as part of the H2020-MSCA-ITN-2016 project PAM^2, Precision Additive Metal Manufacturing, which is funded by The European Union Framework Programe for Research and Innovation—Grant Agreement No. 721383. The authors acknowledge the support provided by the Karlsruhe Nano Micro Facility (KNMF-LMP, http://www.knmf.kit.edu/), a Helmholtz research infrastructure at Karlsruhe Institute of Technology (KIT), Germany. The authors also gratefully acknowledge the support of Dr. Tawheed Hashem from the Institute of Functional Interfaces (IFG) of the KIT, Germany who performed the microscopy for the SEM images that are discussed in this paper. The authors also thank Mr. Florian Messerschmidt of the Institute for Micro Process Engineering (IMVT) of the KIT, Germany for helping prepare the cross cuts for optical microscopy.

Appendix A. Supporting information

Supplementary data associated with this article can be found in the online version at doi:10.1016/j.addma.2021.102148.

References

[1] I. Yadroitsev, I. Yadroitsava, A. Du Plessis, 2 - Basics of laser powder bed fusion, in: I. Yadroitsev, I. Yadroitsava, A. du Plessis, E. MacDonald (Eds.), Fundamentals of Laser Powder Bed Fusion of Metals, Elsevier, 2021, pp. 15–38.
[2] J. Savolainen, M. Collan, How additive manufacturing technology changes business models? – review of literature, Addit. Manuf. 32 (2020), 101070.
[3] E. Lopez, F. Brueckner, S. Gruber, 21 - Industrial applications, in: I. Yadroitsev, I. Yadroitsava, A. du Plessis, E. MacDonald (Eds.), Fundamentals of Laser Powder Bed Fusion of Metals, Elsevier, 2021, pp. 583–595.
[4] M. Bayat, A. Thanki, S. Mohanty, A. Witvrouw, S. Yang, J. Thorborg, N.S. Tiedje, J. H. Hattel, Keyhole-induced porosities in Laser-based Powder Bed Fusion (L-PBF) of Ti6Al4V: High-fidelity modelling and experimental validation, Addit. Manuf. 30 (2019), 100835.
[5] J.C. Snyder, K.A. Thole, Understanding laser powder bed fusion surface roughness, J. Manuf. Sci. Eng. Trans. Asme 142 (7) (2020).
[6] A.E. Patterson, S.L. Messimer, P.A. Farrington, Overhanging features and the slm/dmls residual stresses problem: review and future research need, Technologies 5 (2) (2017) 15.
[7] P. Mercelis, J.P. Kruth, Residual stresses in selective laser sintering and selective laser melting, Rapid Prototyp. J. 12 (5) (2006) 254–265.
[8] E. Maleki, S. Bagherifard, M. Bandini, M. Guagliano, Surface post-treatments for metal additive manufacturing: Progress, challenges, and opportunities, Addit. Manuf. 37 (2021), 101619.
[9] A. Charles, A. Elkaseer, L. Thijs, V. Hagenmeyer, S. Scholz, Effect of process parameters on the generated surface roughness of down-facing surfaces in selective laser melting, Appl. Sci. 9 (6) (2019) 1256.
[10] D. Thomas, R. Bibb, Identifying the geometric constraints and process specific challenges of selective laser melting, Proceedings of Time Compression Technologies Rapid Manufacturing Conference, Coventry, United Kingdom, 2008.
[11] J. Jhabvala, E. Boillat, C. Andre, R. Glardon, An innovative method to build support structures with a pulsed laser in the selective laser melting process, Int J. Adv. Manuf. Technol. 59 (2012) 137–142.
[12] X. Wang, K. Chou, Effect of support structures on Ti-6Al-4V overhang parts fabricated by powder bed fusion electron beam additive manufacturing, J. Mater. Process. Technol. 257 (2018) 65–78.
[13] F. Calignano, Design optimization of supports for overhanging structures in aluminum and titanium alloys by selective laser melting, Mater. Des. 64 (2014) 203–213.
[14] A. Elkaseer, A. Charles, S. Scholz, Development of Precision Additive Manufacturing Processes, in: R.K. Leach, S. Carmignato (Eds.), Precision Metal Additive Manufacturing, CRC Press, Boca Raton, 2021.
[15] M. Markl, C. Korner, Multiscale modeling of powder bed-based additive manufacturing, Annu. Rev. Mater. Res. 46 (1) (2016) 93–123.
[16] M. Bayat, A. Thanki, S. Mohanty, A. Witvrouw, S.F. Yang, J. Thorborg, N.S. Tiedje, J.H. Hattel, Keyhole-induced porosities in laser-based powder bed fusion (L-PBF) of Ti6Al4V: high-fidelity modelling and experimental validation, Addit. Manuf. 30 (2019), 100835.
[17] K. Cooper, P. Steele, B. Cheng, K. Chou, Contact-free support structures for part overhangs in powder-bed metal additive manufacturing, Inventions 3 (1) (2018) 2.
[18] U. Paggi, R. Ranjan, L. Thijs, C. Ayas, M. Langelaar, A. van Keulen, B. van Hooreweder, New support structures for reduced overheating on downfacing regions of direct metal printed parts, 30th Annual International Solid Freeform Fabrication Symposium, University of Texas, 2019.
[19] A.J.M. Driessen, Overhang constraint in topology optimisation for additive manufacturing: A density gradient based approach, Delft University of Technology, Delft, The Netherlands, 2016.
[20] A. Garaigordobil, R. Ansola, J. Santamaria, I.F. de Bustos, A new overhang constraint for topology optimization of self-supporting structures in additive manufacturing, Struct. Multidiscip. Optim. 58 (5) (2018) 2003–2017.
[21] R. Ranjan C. Ayas M. Langelaar F. Keulen Towards design for precision additive manufacturing: A simplified approach for detecting heat accumulation. in: Proceedings of the ASPE and EUSPEN Summer Topical Meeting, 2018.
[22] S. Sun, M. Brandt, M. Easton, Powder bed fusion processes, in: M. Brandt (Ed.), Laser Additive Manufacturing, Woodhead Publishing, 2017, pp. 55–77.
[23] A. Khorasani, I. Gibson, U.S. Awan, A. Ghaderi, The effect of SLM process parameters on density, hardness, tensile strength and surface quality of Ti-6Al-4V, Addit. Manuf. 25 (2019) 176–186.
[24] W.E. King, H.D. Barth, V.M. Castillo, G.F. Gallegos, J.W. Gibbs, D.E. Hahn, C. Kamath, A.M. Rubenchik, Observation of keyhole-mode laser melting in laser powder-bed fusion additive manufacturing, J. Mater. Process. Technol. 214 (12) (2014) 2915–2925.
[25] C.Y. Yap, C.K. Chua, Z.L. Dong, Z.H. Liu, D.Q. Zhang, L.E. Loh, S.L. Sing, Shotgun proteomic analysis of tiger milk mushroom (Lignosus rhinocerotis) and the isolation of a cytotoxic fungal serine protease from its sclerotium, J. Ethnopharmacol. 174 (2015) 437–451.
[26] J. Han, J.J. Yang, H.C. Yu, J. Yin, M. Gao, Z.M. Wang, X.Y. Zeng, Microstructure and mechanical property of selective laser melted Ti6Al4V dependence on laser energy density, Rapid Prototyp. J. 23 (2) (2017) 217–226.
[27] Y. Liu, J. Zhang, Z.C. Pang, W.H. Wu, Investigation into the influence of laser energy input on selective laser melted thin-walled parts by response surface method, Opt. Lasers Eng. 103 (2018) 34–45.
[28] M. Marrey, E. Malekipour, H. El-Mounayri, E.J. Faierson, A Framework for optimizing process parameters in powder bed fusion (PBF) process using artificial neural network (ANN), Procedia Manuf. 34 (2019) 505–515.
[29] U. Scipioni Bertoli, A.J. Wolfer, M.J. Matthews, J.-P.R. Delplanque, J. M. Schoenung, On the limitations of volumetric energy density as a design parameter for selective laser melting, Mater. Des. 113 (2017) 331–340.
[30] F. Caiazzo, V. Alfieri, G. Casalino, On the relevance of volumetric energy density in the investigation of inconel 718 laser powder bed fusion, Materials 13 (3) (2020) 538.
[31] A.H. Maamoun, Y.F. Xue, M.A. Elbestawi, S.C. Veldhuis, Effect of selective laser melting process parameters on the quality of Al alloy parts: powder characterization, density, surface roughness, and dimensional accuracy, Materials 11 (12) (2018) 2343.
[32] J. Pegues, M. Roach, R.S. Williamson, N. Shamsaei, Surface roughness effects on the fatigue strength of additively manufactured Ti-6Al-4V, Int. J. Fatigue 116 (2018) 543–552.
[33] S.M.J. Razavi, B. Van Hooreweder, F. Berto, Effect of build thickness and geometry on quasi-static and fatigue behavior of Ti-6Al-4V produced by electron beam melting, Addit. Manuf. 36 (2020), 101426.
[34] M. Shange, I. Yadroitsava, A. du Plessis, I. Yadroitsev, Roughness and near-surface porosity of unsupported overhangs produced by high-speed laser powder bed fusion, 3D Print. Addit. Manuf. 0 (0) (2021) (null).
[35] A. Townsend, N. Senin, L. Blunt, R.K. Leach, J.S. Taylor, Surface texture metrology for metal additive manufacturing: a review, Precis. Eng. J. Int. Soc. Precis. Eng. Nanotechnol. 46 (2016) 34–47.
[36] J. Robinson, I. Ashton, P. Fox, E. Jones, C. Sutcliffe, Determination of the effect of scan strategy on residual stress in laser powder bed fusion additive manufacturing, Addit. Manuf. 23 (2018) 13–24.
[37] R. Mertens, S. Clijsters, K. Kempen, J.P. Kruth, Optimization of scan strategies in selective laser melting of aluminum parts with downfacing areas, J. Manuf. Sci. Eng. -Trans. Asme 136 (6) (2014), 061012.
[38] A. Charles, A. Elkaseer, L. Thijs, S.G. Scholz, Dimensional errors due to overhanging features in laser powder bed fusion parts made of Ti-6Al-4V, Appl. Sci. 10 (7) (2020) 2416.
[39] L. Thijs, F. Verhaeghe, T. Craeghs, J.V. Humbeeck, J.-P. Kruth, A study of the microstructural evolution during selective laser melting of Ti–6Al–4V, AcMat 58 (9) (2010) 3303–3312.
[40] I. Yadroitsev, A. Gusarov, I. Yadroitsava, I. Smurov, Single track formation in selective laser melting of metal powders, J. Mater. Process. Technol. 210 (12) (2010) 1624–1631.
[41] J.P. Oliveira, T.G. Santos, R.M. Miranda, Revisiting fundamental welding concepts to improve additive manufacturing: from theory to practice, Prog. Mater. Sci. 107 (2020), 100590.